Infrared Remote Sensing for Quantifying River Thermal Heterogeneities and sensors comparison

Auteur : François, Yohann
Promoteur(s) : Georges, Blandine; Michez, Adrien
Faculté : Gembloux Agro-Bio Tech (GxABT)
Diplôme : Master en bioingénieur : sciences et technologies de l'environnement, à finalité spécialisée
Année académique : 2019-2020
URI/URL : http://hdl.handle.net/2268.2/9508

LIÈGE université
Gembloux
Agro-Bio Tech

INFRARED REMOTE SENSING FOR QUANTIFYING RIVER THERMAL HETEROGENEITIES AND SENSORS COMPARISON

FRANCOIS YOHANN

MASTER THESIS PRESENTED IN ORDER TO OBTAIN THE BIOENGINEER MASTER DIPLOMA ORIENTATION SCIENCES AND TECHNOLOGIES OF ENVIRONMENT

ACADEMIC YEAR 2019 - 2020

SUPERVISORS : DR ADRIEN MICHEZ & BLANDINE GEORGES

LIÈGE université
Gembloux
Agro-Bio Tech

INFRARED REMOTE SENSING FOR QUANTIFYING RIVER THERMAL HETEROGENEITIES AND SENSORS COMPARISON

FRANCOIS YOHANN

MASTER THESIS PRESENTED IN ORDER TO OBTAIN THE BIOENGINEER MASTER DIPLOMA ORIENTATION SCIENCES AND TECHNOLOGIES OF ENVIRONMENT

ACADEMIC YEAR 2019 - 2020

SUPERVISORS : DR ADRIEN MICHEZ & BLANDINE GEORGES

Acknowledgements

Tout d'abord, j'aimerais remercier mes promoteurs Blandine Georges et Adrien Michez pour m'avoir donné l'opportunité de travailler sur un sujet qui me passionne ainsi que leurs conseils.

Merci à Baptiste Marteau pour sa collaboration, ses précieuses informations sur la démarche expérimentale et son expérience dans le domaine.

Je tiens également à remercier mon papa. Il m'a toujours soutenu dans les moments difficiles, sans lui je ne serai jamais arrivé aussi loin. Ses larges connaissances ainsi que son tempérament hors du commun font de lui une personne exceptionnelle.

J'aimerais remercier de tout coeur ma grande tante qui, durant mes études, a été d'une aide infinie. Sa gentillesse et sa volonté de fer seront toujours, pour moi, une source d'inspiration et de motivation.

Un tout grand merci à mon rôti, pour son aide et les bons moments qui ont adouci cette épreuve compliquée et confinée. Merci également à Mouchette, de m'avoir accueilli les bras ouvert, c'est quelque chose que je n'oublierai jamais.

Enfin, j'aimerais remercier l'ensemble de mes amis (il y a beaucoup trop de monde à citer) avec qui j'ai partagé ces années d'études. La Faculté des Sciences Agronomiques de Gembloux restera un souvenir inoubliable, et j'espère (c'est une certitude) revoir mes camarades noir et vert à l'occasion.

Abstract

English

Water temperature is a key parameter in aquatic ecosystems controlling chemical and physical processes. These essential ecosystems have been threatened for many years by increasing anthropogenic pressure and worrying climate change. Existing data of water temperature are generally derived from thermometers which, although accurate, have very low spatial resolution. Fortunately, the development of new technologies has made it possible to apply new methods of temperature measurement such as remote sensing by infrared thermography. The high spatial resolution offered by this technology allows to study thermal heterogeneities and consequently to learn more about the functioning of watercourses by determining factors influencing its temperature. Therefore, the objectives of this work consisted firstly in using a method of remote sensing by infrared thermography to highlight the spatial thermal variability of water in the environment of a river. Secondly, to compare the results from two different thermal cameras, and finally to compare the measurements from infrared thermography with a classical *in situ* temperature measurement by thermometers.

French

La température de l'eau est un paramètre clé des écosystèmes aquatiques régissant les processus chimiques et physiques de la rivière. Ces écosystèmes essentiels sont, depuis de nombreuses années, menacés par une pression anthropique de plus en plus forte et un dérèglement climatique inquiétant. Les données existantes concernant la température de l'eau sont généralement issues de thermomètres qui, bien qu'ils soient précis, présentent une très faible résolution spatiale. Heureusement, le développement de nouvelles technologies a permis l'application de nouvelles méthodes de mesure de la température telle que la télédétection par thermographie infrarouge. La haute résolution spatiale offerte par cette technologie permet d'étudier l'hétérogénéité thermique afin d'en apprendre davantage sur le fonctionnement du cours d'eau en observant ce qui influence sa température. Dès lors, les objectifs de ce travail ont consisté premièrement à utiliser une méthode de télédétection par thermographie infrarouge afin de mettre en évidence la variabilité thermique spatiale de l'eau dans l'environnement d'une rivière. Deuxièmement, de comparer les résultats de deux caméras thermiques différentes, et enfin de comparer les mesures issues de la thermographie infrarouge avec une mesure classique *in situ* de la température par des thermomètres.

Contents

List of Figures

List of Tables

Chapter 1

Introduction

1.1 Stream temperature : definition and impact on aquatic ecosystems

Stream water temperature is an environmental factor of the aquatic ecosystem with significant impact on all ecological processes. Water temperature influences the physical properties of watercourses (Pautou et al., 2003). It affects the nutrient cycle (Chang et al., 2015), the solute concentration (Poole and Berman, 2001; Johnson and Jones, 2000), the solubility of gases in water such as oxygen (Antonopoulos and Gianniou, 2003), the dissociation of dissolved salts, the chemical and biochemical reactions as well as the development and growth of organisms living in water (Demba et al., 2013). Moreover, this factor reflects the balance of atmospheric heat exchange at the air-water interface (Caldwell et al., 2019).

Hence, water temperature influences a large panel of aquatic organisms from invertebrates to salmonids (Caissie, 2006). Regarding fishes, this factor affects the overall biological development (Kupren et al., 2008). Indeed, it can impact their processes of migration cues and egg maturation (Jonsson and Jonsson, 2018) but also, spawning and incubation success, growth, and general stress which relates to intra-specific competition and susceptibility to parasites and diseases (Lackenby et al., 2007), despite other regulatory factors coming into play (Kupren et al., 2008). Each species has a specific heat tolerance varying according to its stage in the life cycle (Georges et al., 2019; Marsh et al., 2005). Ectothermic organisms (such as fishes and macroinvertebrates) are directly impacted because their internal body temperature is regulated by the temperature of surrounding environment (Marsh et al., 2005). For example, the brown trout (*Salmo trutta fario L.*) is a commun

species present on Walloon territory that thrives within a temperature range of 4 to 19 °C. This temperature of comfort, at which the animal evolves with minimal stress, is called thermal preferendum. Outside of this temperature range, individuals are under stress, leading to death when water temperature exceeds 25 °C (lethal temperature) (Georges et al., 2019).

This is why, stream water temperature is a key parameter that controls all chemical and biological processes within the river channel (Wawrzyniak et al., 2012; Dugdale, 2016). It is therefore essential to measure the water temperature with the utmost accuracy (Demba et al., 2013).

1.2 Drivers influencing stream water temperature

Stream water temperature depends on a wide range of drivers [figure 1.1] (Wawrzyniak et al., 2013; Caissie, 2006; Webb et al., 2008) which can be grouped into two categories: first, natural variations like atmospheric conditions, riparian vegetation or topography (directly linked to the fluvial stream structure) and secondly, anthropogenic perturbations such as thermal pollution, climate change and deforestation (Johnson and Jones, 2000; Caissie, 2006). Interactions between internal structure of stream and external drivers influence channel water temperature (Poole and Berman, 2001). External drivers (such as atmospheric conditions) regulate the net heat energy and water delivered to a stream. The internal structure of a river [figure 1.2] determines how heat and water are distributed within the watercourse, and regulates the heat exchanges between the different components (channel, alluvial aquifer, and riparian zone/floodplain) (Poole and Berman, 2001).

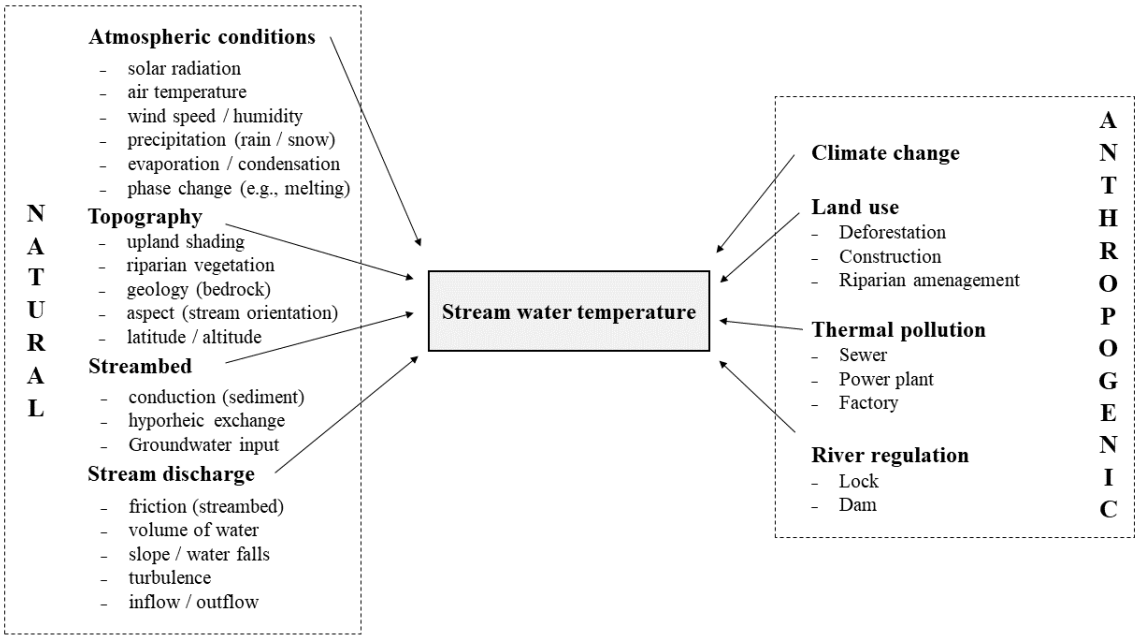

Figure (1.1) Factors influencing stream water temperature of rivers
Adapted from (Caissie, 2006)

1.2.1 Natural variations

There are many natural factors influencing stream temperature (Caissie, 2006). Some of them will be reviewed to get a better understanding of the thermal phenomena of a river. Firstly, the internal structure of the watercourse. The stream structure can be defined by, at least, three integrated and interdependent components : the riparian zone, the channel and the alluvial aquifer [figure 1.2] (Poole and Berman, 2001). Stream systems are particularly complex and diverse, comprising a mosaic of ecosystems and their numerous interactions (Dugdale et al., 2015).

For several years, many studies have shown the significance and complexity of water exchanges between alluvial aquifer and channel (Wawrzyniak et al., 2013; Buffington and Tonina, 2009; Tockner et al., 2006). Hyporheic groundwater is defined as water localized in the porous sediments of a river (Tonina and Buffington, 2009), and phreatic groundwater is located below the water table (Wawrzyniak et al., 2013). Hyporheic and phreatic exchanges have considerable impacts on water temperature patterns and are directly linked to the fluvial stream structure (Wawrzyniak et al., 2013). Exchanges between these two kinds of water occur at different temporal and spatial scales (Poole and Berman, 2001). Generally during summer, phreatic groundwater temperature fluctuates less than river wa-

ter and therefore have a cooling effect on the river (Wawrzyniak et al., 2013). Wawrzyniak et al (2013) also observed that the morphology of the watercourse affects water temperature. Indeed, the braided river is composed of areas with different characteristics, such as flow differences, that are responsible for a modification of watercourse temperature. For exemple, when the water stagnates and is less well mixed with the rest of the current, it heats up easily due to its exposure to the sun (Sinokrot and Gulliver, 2000).

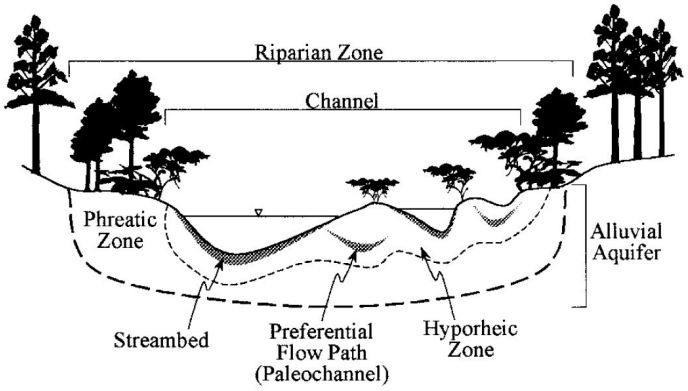

Figure (1.2) Structural components of a stream system
(Poole and Berman, 2001)

Secondly, atmospheric conditions are one of the most important natural factors influencing water temperature. Indeed, it is responsible for heat exchange process at the surface including phase change (Caissie, 2006). For example the effect of solar radiations has a significant warming impact on stream water temperature. An increase in riparian vegetation reduces solar radiation absorbed by the water which leads to mitigated water temperature. In fact, shadows lead to decrease water temperatures by reducing the direct heating of water surface through solar radiation (Roth et al., 2010; Marsh et al., 2005). At the opposite, the presence of a dense canopy cover can reduce the cooling at night by decreasing the radiant heat loss from water. (Marsh et al., 2005).

1.2.2 Anthropogenic variations

Human activities influence stream water temperature in various ways and have been the subject of numerous studies in recent years. Among those anthropogenic activities, the riparian land use can be mentioned since it includes the deforestation (Moore et al., 2005), the thermal pollution (Miara et al., 2018), the river regulation (Webb et al., 2008), etc which are responsible for important thermal hétérogénéities in rivers (Wawrzyniak et al., 2013). As mentioned in the previous section, the deforestation reduces the vegetation sourrounding rivers, impacting considerably the solar radiations absorbed by water (Caissie, 2006). Regarding the thermal pollution, it has been demonstrated that the intensive use of water from rivers as cooling system in power plants increases the stream temperature, since the released water is warmer (Miara et al., 2018). Moreover, the diversions, dams and impoundments change the river flow rate and consequently the internal water mixing which induce temperature variations (Hamblin and McAdam, 2003).

Another considerable threat for aquatic ecosystems is the climate change, a direct consequence of human activities (Quilbé et al., 2008). During the 21st century, stream water temperature will increase by an average of (1-3 C°) depending on the scenario and the location on earth (Durance and Ormerod, 2007; Palmer et al., 2009). Climate change has been recognized as an important source of disturbance (Sinokrot and Stefan, 1993), that would significantly modify the distribution of aquatic organisms and the dynamic of temperature (Caissie, 2006). Indeed, several mechanisms such as the direct sensible heat transfer, the long-wave atmospheric radiation and the heating of groundwater are influenced by the anthropogenic climate change and affect the stream temperature. Consequently, aquatic communities have to shift to look for thermally adapted habitat (Isaak et al., 2012). Although many species could persist after a 3 C° increase in water temperature, the most sensitive species (between 5-12 percent of the pool) would risk extinction (Durance and Ormerod, 2007).

The ability to map river temperature is therefore important for locating the impacts of thermal variations, and try to understand the causes. (Dugdale et al., 2019). Indeed, a greater grasp of stream temperature variations is essential to preserve rivers against modifications induced by humans (Qiu et al., 2020; Leibowitz et al., 2014).

1.3 Spatial and temporal variability

The impact of the natural and anthropogenic variations and on overall thermal conditions of rivers varies spatially within the stream (Caissie, 2006). For example, the interactions between the internal structure and external drivers create variability of stream temperature at spatial and temporal scales (Poole and Berman, 2001). Rivers present a mix of cold and warm zones, which are very variable spatially and temporally (Torgersen et al., 2001; Handcock et al., 2012; Dugdale, 2016). Also, concerning spatial variability, it is often observed that the average daily water temperature increases in a downstream direction (Caissie, 2006). Water temperature is approaching the groundwater temperature at the source and increases as one moves away from it. This trend is not linear and the degree of increase is higher for narrow streams than for large rivers (Caissie, 2006).

On a temporal scale, the stream water temperature fluctuates at every moment. More specifically, studies have looked at particular cycles such as the daily and annual cycle. Generally, daily variations generate a minimum in the early morning (at sunrise) and a maximum in late afternoon to early evening (Caissie, 2006). In addition, rivers have an annual temperature cycle that has the characteristics of a sinusoidal function, with colder temperatures in winter and maximum temperatures in summer (Caissie, 2006).

Therefore rivers present complex thermal heterogeneities, both spatially and temporally. Understanding variabilities of stream water temperature at different scales reveals real difficulties and create a scientific challenge (Wawrzyniak et al., 2013; Webb et al., 2008).

1.4 Conventional temperature measurement

Classically, the technologies and methods using thermometers applied to measure stream water temperature are simple and robust (Langan et al., 2001). For example, two studies used thermometers (connected to dataloggers, placed 10 centimetres below the surface with an accuracy of +/- 0.1 Celsius degree) as temperature reference (Wawrzyniak et al., 2013; Torgersen et al., 2001). This conventional method allows to obtain a punctual measure of stream temperature. The advantage of *in situ* thermometers is that it can stay in place for several years and give accurate data for a long-term experiment (Webb and Nobilis, 2007). It is therefore a relevant method to study the temporal heterogeneity inside a river. (Langan et al., 2001; Webb and Nobilis, 2007; Lundquist et al., 2003).

Nevertheless, the discrete measurements recorded by the thermometers offer poor spatial resolution (Dugdale, 2016). The temporal resolution is good but in contrast, *in situ* thermometers cannot be placed every metre in the stream. Typically, they are placed several hundred meters away from each other (Torgersen et al., 2001). So, monitoring of stream water temperature using thermometers doesn't reflect the health of the stream due to a lack of information for these thermal distributed zones in the river based on wood debris, rocks, shadows of vegetation, and groundwater recharge (Poole and Berman, 2001; Cherkauer et al., 2005). The cold refuge zones, essential for the development of fish, are difficult to detect with this technology (Poole and Berman, 2001). These refugia have temperatures lower than the stream average (3 C° shown in this study (Ebersole et al., 2003)), have spatial limitations, so point observation can completely miss their presence (Poole and Berman, 2001).

Since few years, while the majority of existing river temperature data are based on monitoring from thermometers, there has been recently a need for accurate high spatial resolution data ; which cannot be obtained with the use of thermometers. However thermometers alone can not give such spatial information in terms of measurements (Dugdale, 2016). This lack of information could be solved by the use of infrared thermography (IRT) technology and remote sensing.

1.5 Infrared thermography : IRT

Infrared thermography (IRT) generates surface-temperature mapping by measuring the thermal energy which is emitted by objects in the infrared band of the electromagnetic spectrum [figure 1.3] (Meola and Carlomagno, 2009).

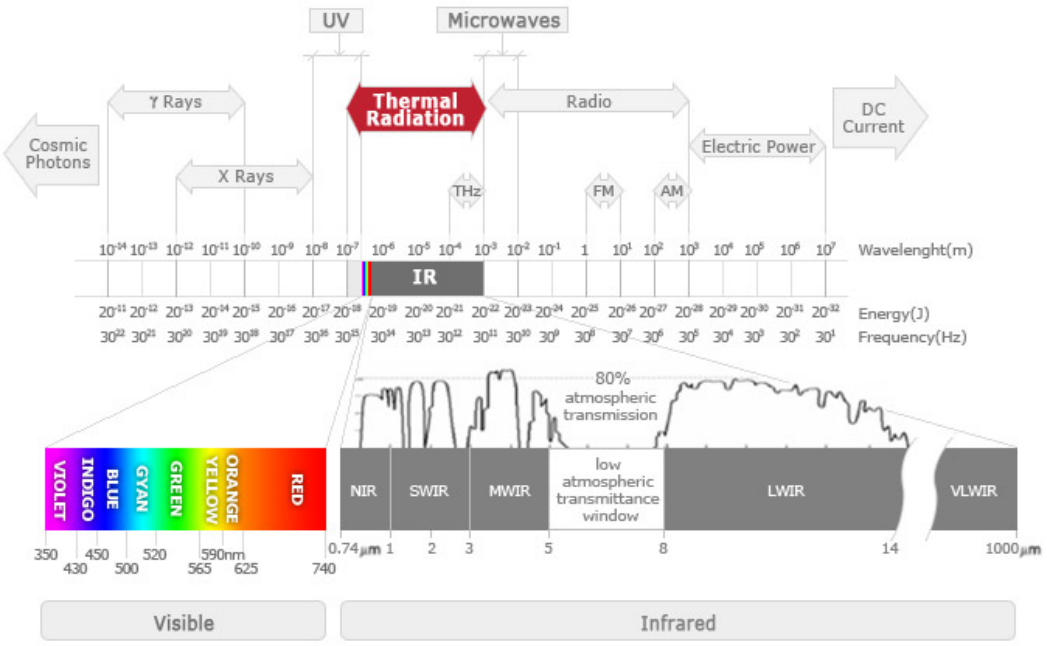

Figure (1.3) Electromagnetic spectrum : wavelengths used by thermographic systems (COX, 2015)

So, infrared thermography is a technique for visualizing the radiative flux of a surface (Arconada et al., 1987). All objects that have surface temperatures above absolute zero emit electromagnetic radiation that can be characterised by two physical parameters; wavelength and intensity. Both of these features are linked by physical laws to the surface temperature of an object. The emitted radiation is a function of the temperature of the material (Usamentiaga et al., 2014) and can be obtained from the equation below :

$$Q_{tot} = \sigma.T^4 \tag{1}$$

Where (Q_{tot}) is the total radiation emitted by a body in $[W.m^{-2}]$, (T) is the temperature of the body in Kelvin $[K]$ and (σ) is the Stefan-Boltzmann constant equal to $5,67.10^{-8}[W.m^{-2}.K^{-4}]$.

It is therefore possible to use the intensity and wavelength of radiation emitted by an object to measure its surface temperature, without physical contact (Speakman and Ward, 1998). Each part of a body (or object) emits its own radiation, so the surface can have differences in radiation depending on temperature. Infrared thermography will allow the representation of these radiation differences by creating an image representation. The IRT measuring sensor (cameras) measures the infrared radiations emitted by the object surface and convert the received energy into temperature [figure 1.5]. The image is reconstructed according to the resolution of the sensors. The resolution is an internal parameter corresponding to the amount of information that camera can acquired, and it is reflected by two parameters: N and M, the number of rows by the number of columns of the matrix (Usamentiaga et al., 2014). Each "cell" of the N x M matrix is called a pixel, and it is the smallest constituent element of the image (shown in blue in the figure [1.5]).

The infrared image is different from the visible image. In the first case the image reflects the radiation emitted by the IR band of the electromagnetic spectrum. While in the second case, it is the visible reflected light [figure 1.3]. In addition, to produce the final result, called thermogram, an additional process is required, which consists in assigning a color to each pixel represent infrared energy level [figure 1.4] (Usamentiaga et al., 2014).

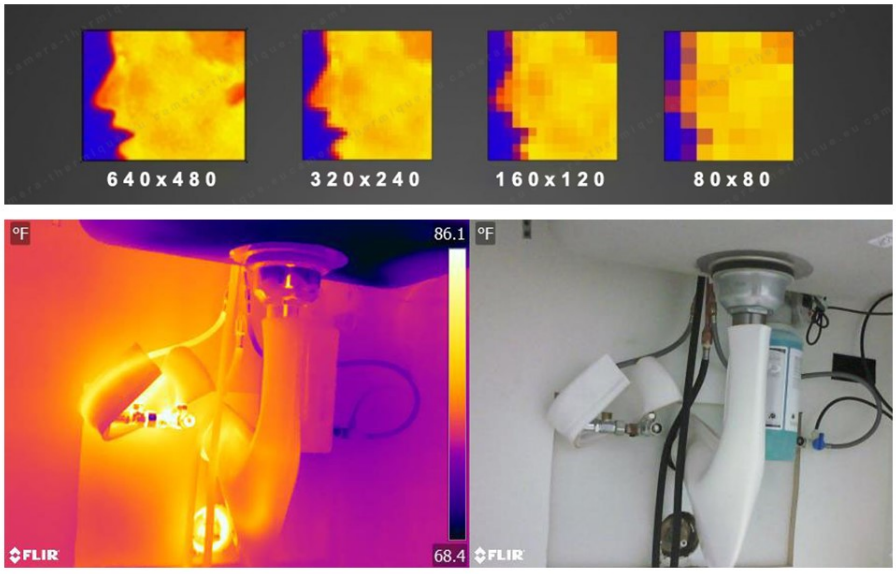

Figure (1.4) Image resolution differences and comparison between IR and visible images (FLI, 2019)

1.5.1 Camera settings

The different characteristics of the sensor will influence the final product which is the thermal image (thermogram). The [figure 1.5] summarizes and simplifies the functionality of a thermal camera by identifying the important technical features. As mentioned previously, the temperature measurement by the sensor is not direct. In fact, a signal processing [figure 1.5 yellow box] transforms the radiation measurement into a temperature measurement (Usamentiaga et al., 2014). In general, this signal processing includes a first transformation to convert the measured radiation into an electrical signal via a correspondence curve. Then, a microprocessor will allow digital signal processing including smoothing, sequencing, correction and interpretation. Finally, a compensation allows to take into account factors that may influence the measurement, and applies a calibration. The final result is a temperature measurement for each pixel corresponding to the spatial resolution of the sensor.

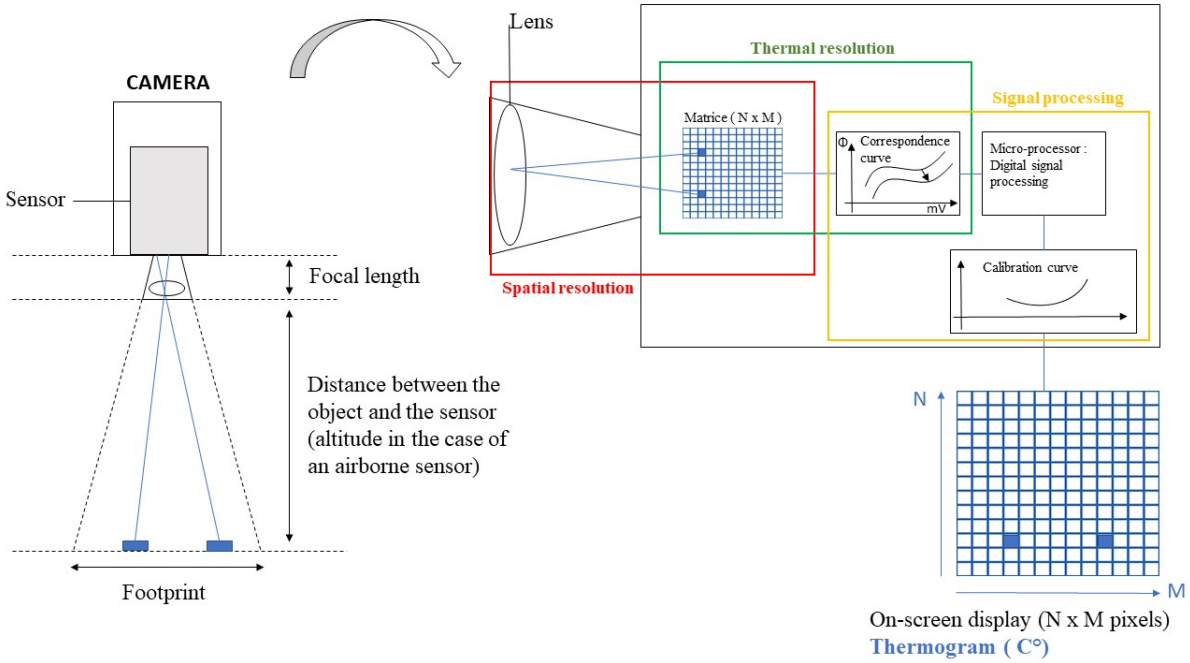

Figure (1.5) Simplified diagram of an infrared camera and technical parameters
Adapted from (Latte et al., 2020; FIT, 2017)

The ground resolution can be calculated with the different parameters shown in [figure 1.5]. The following equation comes from a relationship by the triangle of Thales between the focal distance and the distance to the object to be measured (Latte et al., 2020).

$$\frac{Focal_{length}}{Width_{matrix}} = \frac{Altitude}{Footprint}$$

$$Resolution_{ground} = \frac{Footprint}{M}$$

Where (M) is the number of pixels in the matrix, given by the spatial resolution of the sensor [figure 1.5 red box] and $(Width_{matrix})$ can be calculated by knowing the dimension of a pixel. Ground resolution is an important parameter to take into account when measuring an object or a landscape. The smaller the pixel size on the ground, the higher the resolution and the better is the highlighting of temperature differences within the same image. The pixel size have to be small enough to characterize the typical length scales of interest (Garrigues et al., 2006).

Usually the sensor's footprint is smaller than the area in which the analysis is to be performed. To cover the entire area, several images are required. In order to assemble these images, a number of common points to each image are necessary, so the images are taken with an overlap. The speed of the platform and the speed with which the sensor takes the images therefore defines the percentage of overlap between each image. A fast moving platform therefore needs a sensor that takes pictures quickly. The possibilities of platforms are numerous and are described in the following section.

1.5.2 Platform options

Several platforms can be used to measure stream water temperature by remote sensing IRT : fixed support (tripod), unmanned aerial vehicle (UAV or drone), paraglider, ULM, helicopter, aircraft and satellite. The choice of platform is directly linked to the resolution of the image and therefore to the objectives to be achieved. The higher the altitude, the greater the distance between the surface to be measured and the sensor, thus affecting the ground resolution (see 1.5). Satellite with IRT sensors have the capacity to view large regions instantly (Cherkauer et al., 2005). However, the images recorded from satellites have a generally lower resolution than drones (Wawrzyniak et al., 2013). This is why, in TIR remote sensing, satellites are used to study very large area like land use over entire landscapes of several square kilometres (Weng, 2009). While drone can be used to study smaller targets such as rivers with only a few meters wide (Handcock et al., 2012). The table [1.1] attempts summarize the advantages and disadvantages of using a particular platform and compares them with conventional measurements (section 1.4).

Table (1.1) Comparative table between IRT and in-situ thermometer : Data acquisition

Data acquisition		
	Advantages	Disadvantages
In situ thermometers	• Data can be recorded at any depth in the water section. • Data collection requires low expertise. • Climatic conditions have less impact on the recording measurements. • Connected to the datalogger, this allows continuous measurement over time. • If there is not too much material put in place, the cost can be low.	• Punctual temperature measurements, scattered throughout the stream, so there is no information on spatial variability in the stream. • The material may be destroyed by external factors. • Most of the time, temperature stations are located in larger rivers. • Calibration is still required. • To record spatially measurements, many workforces must be deployed.
Infrared thermography	• *In situ* thermometer network in place can be used for validation. Satellite: • Regional scale coverage, repeat monitoring with systematic image characteristics, with low cost. • Data can be generated with multiple scales from local to regional. Plane: • Can measure TIR images at finer pixel sizes than satellites and can be suitable for narrower streams and rivers. • Can travel a great distance in a short period of time. Helicopter: • Can measure TIR images at finer pixel sizes than plane and can be suitable for narrower streams and rivers (it's directly linked of flight altitude and speed). • Less demanding for take-off procedures UAV: • Lower cost than other airborne (plane or helicoptere). • Facilities to fly and record data quickly. • Lowest speed and flight altitude : can measure TIR images at finer pixel sizes than helicopter and can be suitable for narrower rivers. Ground: • Materiel is easy to place and validate; requires physical access to the river. • High quality images because the platform does not move.	• The price of TIR images can be high (Plane and helicopter). • Complex measurement. • Limitation in time. • Data recorded outside the NADIR (see 1.5.4 section : surface reflections). Satellite: • Cloud layer makes the TIR images unavailable. Plane: • Acquired over narrow swath widths covering small areas in comparison to satellite data. • Acquisition can be expensive, especially if multiple scan lines are needed to generate a mosaic of TIR images. • High flight speed. • Flight regulations of the areas concerned. Helicopter: • Acquisition costs can be high (like plane). • Noisy. • Flight regulations of the areas concerned. UAV: • The life of the battery resulting in a short flight period and therefore a small area overflown. • Flight regulations of the areas concerned. Ground: • Just view data from specific locations spot along the river. • The reflected radiation from objects in the river needs to be reduced. The viewing angles need to be carefully selected.

Adapted from (Handcock et al., 2012)

1.5.3 Remote sensing in the context of a watercourse study

Infrared thermography by remote sensing allows the rapid and high-resolution characterization of the surface temperature of different environments and large areas like rivers (Handcock et al., 2006; Torgersen et al., 2001). It is therefore interesting to use this technology to fill the lack of information on the spatial thermal heterogeneity of rivers. This technique is increasingly used in the river field but its application in the framework of restoration monitoring remains limited.

The first studies on IRT applied in the framework of river studies date from the 1970s (Atwell et al., 1971). However, the growing interest of scientists was only triggered in the 2000s, in particular thanks to new technologies improving the quality of images and simplifying flights (Maus et al., 2001; Torgersen et al., 2001). Airborne IRT remote sensing allows to identify pollution sources from thermal anomalies such as hot water discharges (Chen et al., 2003). It also allows the search for cold water sources in particular groundwater inflow (Dugdale et al., 2015; Wawrzyniak et al., 2016), and assess the diversity of thermal habitats like local refuge areas in braided rivers (Wawrzyniak et al., 2013). And finally, to describe the "thermal landscape" of a river up to several dozen kilometres and assess its evolution over time or seasons (Handcock et al., 2012).

1.5.4 Sources of error and precautions in river environments

IRT measurement by remote sensing can be subject to many sources of error. In this section, the goal is to present those that are most prevalent in previous studies. This assessment was made in order to learn more about what can influence the IRT measurement. Firstly, it is necessary to pay attention to pixels covering several habitats (called: "mixed pixels") (Dugdale, 2016). This error is really common and happens when the resolution is low. Therefore the temperature reflects not a single kind of surface. The temperature measurement is strongly biased on riverside in the case of low resolution and narrow watercourse (Handcock et al., 2006). Another common source of error is the shadow cast by shoreline objects (such as trees) on the water surface. However, small errors resulting from the close environment of the side are unlikely to introduce a large error when examining water temperature profile at the river scale (Dugdale, 2016).

Furthermore, there are other factors that influence measurement of temperature : emissivity, IRT reflection, atmospheric absorption and surface characteristics (Smith et al., 1996; Torgersen et al., 2001).

1) Emissivity : The emmissivity of a body (for a given wavelength) is defined as the proportion between the radiation emitted by this body and the radiation that would be emitted by a black body at the same temperature. A real object emits only a part of the thermal energy radiated by a blackbody at equal temperature. A grey body has the particularity of having a constant emissivity independent of its wavelength. Reals bodies (normal objects) do not have this characteristic; so, they cannot be considered as greybodies. However, it is usually admitted that for short wavelength intervals, the emissivity can be considered as a constant, and Stephan-Boltzman formula works (Usamentiaga et al., 2014). In most of cases, water areas behave as good radiators with an emissivity coefficient close to 1 (0.97-0.99) for angles between 0 and 30° from NADIR (opposite the zenith and vertically downward from the observer). Outside this angle range, the emissivity factor is reduced and the physical law doesn't work with an impact on measurements. As the temperature measurement is dependent on this factor, a change in this factor inevitably influences the measurement of the radiant temperature recorded by the IRT sensor. Studies (Torgersen et al., 2001; Kay et al., 2005) have shown that this bias can lead to an error of 0.5°C (Dugdale, 2016). Other factors can influence and reduce the emissivity and lead to a loss of accuracy such as: agitation on the water surface, the presence of tannins or turbidity (Dugdale, 2016).

2) Absorption : Atmospheric absorption is the amount of radiation intercepted by the atmosphere including X-rays, ultraviolet and infrared radiation emitted by the sun, except visible light. This is one of the most important characteristics to be taken into account when measuring a surface temperature by TIR and the state of the atmosphere. (Dugdale, 2016; Torgersen et al., 2001; Handcock et al., 2012). Atmospheric conditions can induce a considerable bias, as the presence of water vapour and other suspended atmospheric constituents (smoke, dust) emit radiation in the IRT spectrum (Dugdale, 2016). The altitude will obviously vary this effect on the measurement, the atmospheric distortion is a function of the distance between the sensor and the object whose temperature is to be measured (Dugdale, 2016). Even if the measurement is performed at low altitude, atmospheric humidity is the biggest source of error for IRT measurement (Handcock et al., 2012). The contribution of the composition of the atmosphere and its interaction with the IR spectrum are complex to quantify (Dugdale, 2016). Therefore radiative transfer models exist and are implemented directly in modern IRT cameras. This correction factor

called "transmissivity" allows to correct the temperature measurements (Dugdale, 2016).

3) Surface reflections : Surface reflection can induce a bias in the IRT temperature measurement (by influencing emissivity like mentioned before) but also by reflecting solar radiation and IRL radiation from the sky. This phenomenon occurs at oblique angles, and deteriorates the sensor measurement (Torgersen et al., 2001). However, the choice of a IRT device can reduce the impact of solar reflection (Dugdale, 2016). The long wave radiation coming from the sky is less easily to attenuate because this radiation is in the same range as water (Dugdale, 2016). Some objects on the banks can also influence the measurement, such as riparian vegetation (trees), which can induce an error in surface water temperatures of 0.1-0.6°C (Handcock et al., 2012).

Measurement by infrared thermography has a significant limitation that can be a problem in some studies. IRT sensors only measure the surface temperature of an object in the upper 100 µm of the water column (Dugdale, 2016). This measurement gives no information on the thermal stratification that may be present within the water body. However, this stratification is strongly present for lakes and marine environments, but it is less important in rivers where there is a turbulent flow which creates well-mixed water (Dugdale, 2016).

Chapter 2

Objectives

This work has three main objectives :

1. The comparison between two different thermal cameras for the same experimental protocol and the identification of the differences between these two sensors.
2. The comparison between IRT measurements and conventional *in-situ* thermometer measurements.
3. The establishment of a longitudinal thermal profile of a portion of the river in order to assess its spatial variability. Interpretation of images from infrared remote sensing to analyse thermal heterogeneity inside the stream.

Chapter 3

Materials and methods

3.1 Study area

The Arroux is a river localized in the departments of Côte-d'Or and Saône-et-Loire, in the Bourgogne-Franche-Comté region [figure 3.1]. The length of the Arroux River is 130 kilometres and crosses 32 municipalities of France. The watershed of Arroux is located between three major French rivers: the Loire (of which it is part), the Rhône (to the east) and the Seine (to the north). This river, which drains an area of 3166 square kilometres, originates at the outflow from Muisson pond and flows southwest until it ends up in the Loire river near Digoin. Its depth ranges from 18 centimetres to 4 metres, and altitude from 420 to 220 metres above the sea level. The highest points are in the Morvan massif, which forms the natural dividing line between the Loire and the Seine. The watercourses of the Arroux watershed belong to the degraded oceanic (sandy meandering rivers) domain and are low-energy streams (Jacob-Rousseau et al., 2016). The study area includes a portion of approximately 35 km of the Arroux River [figure 3.1].

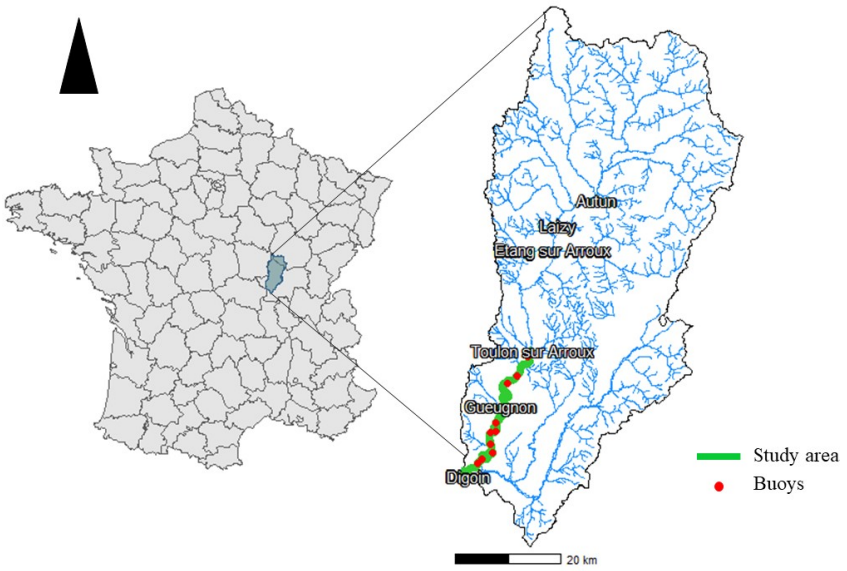

Figure (3.1) Localisation of study area

The flow regimes of the Arroux are highly contrasted, showing abundance in the winter season and a marked low water level in the summer resulting from evapotranspiration and drought [figure 3.2] (Jacob-Rousseau et al., 2016).

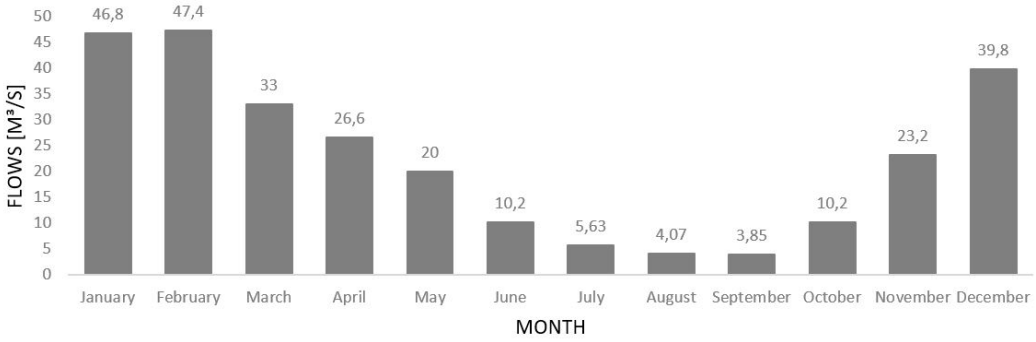

Figure (3.2) Average monthly Arroux flows from 1967 to 2015
(Jacob-Rousseau et al., 2016)

The potentially energetic character of the sandy rivers, of which the Arroux is a part, is conducive to the appearance of thermal variability. Indeed, the water will be less well mixed than in a narrow river with a strong water flow. Moreover, this character will be accentuated in summer during hot and dry events where areas of stagnant water may appear.

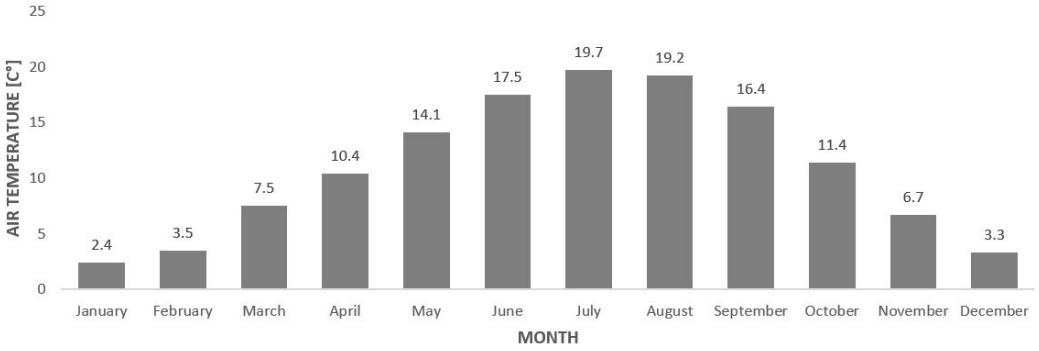

Figure (3.3) Average monthly Arroux air temperature from 1982 to 2012 (CLI, 2012)

The climate of the area is characteristic of a temperate European climate with average temperatures following an annual cycle [figure 3.3]. The water temperature will follow this sinusoidal trend in air temperature (Caissie, 2006). In terms of rainfall, February is the driest month with an average (1982-2012) of 46 mm, while June is the wettest with 83 mm (CLI, 2012).

3.2 Data Acquisition

3.2.1 Airborne images

The flights were conducted in an ULM equipped with a platform holding three sensors: a conventional digital camera (DSC) and two thermal cameras [figure 3.4]. The support of these sensors is fixed thanks to a system of "silent block", making it possible to reduce the vibrations very often at the origin of blurred photos [figure 3.4(b)]. The sensor allowing to take pictures in the visible range was a Nikon D7000 with a 50 mm lens. Two cameras were used and worked independently for thermal imaging :

1) VarioCAM® HR Research : (Infratec, 640 x 480 pixels) with a standard lens (30 mm). This camera measures in the infrared range at wavelengths between 7.5 and 14 µm. It is capable of measuring temperature differences within the same image of around 0.3°C. The measuring accuracy provided by the manufacturer is ± 1°C (or ± 1 % of the displayed value).

2) FLIR VUEPRO R : (640 x 512 pixels) with a lens (9 mm). This camera measures in the infrared range at wavelengths between 7.5 and 13.5 µm. The measuring accuracy provided by the manufacturer is ± 5°C (or ± 5 % of the displayed value).

(a) (b)

Figure (3.4) Flight system
(a) Example of ULM used for image acquisition ; (b) Zoom on the sensor support / Marteau Baptiste © July 10 2018

The flight took place on July 24th 2019, between 4:00 pm and 5:40 pm, with an average altitude of 413 meters. The line of river overflown by the ULM was 35.1 km long, and the area covered by the images was 12.4 km². For the visible, each pixel was constructed with at least 4 images. The ultralight made one outward and one return flight covering the portion of the watercourse with the buoys [figure 3.7]. Flying conditions were good, with clear but very hot weather. As shown in [figure 3.5], air mean temperature during the flight was 38 °C, which is well above the seasonal average shown in [figure 3.3]. The wind was light with peaks of up to 10 km/hour.

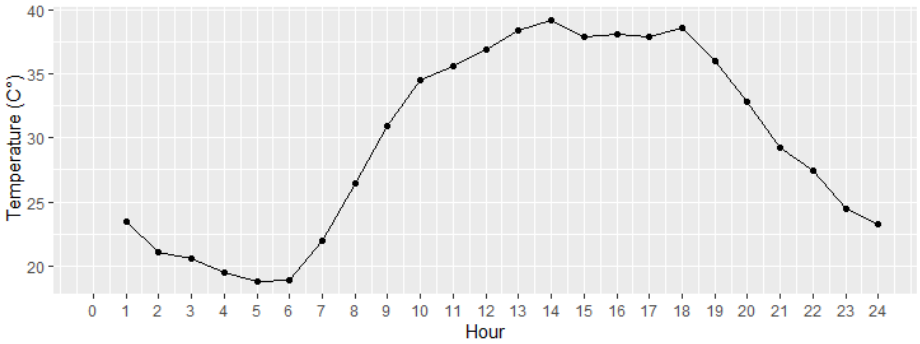

Figure (3.5) Average Arroux air temperature per hour : July 24 2019

3.2.2 Thermometers

At the same time, VEMCO© Minilog temperature recorders (accuracy 0.1°C between 5 and 35°C, uncertainty 0.3°C) were placed on the study line to measure *in situ* water surface temperature. For this purpose, the thermometers were attached to the buoys [figure 3.6]. The buoys have an id (letter F + number) to identify them. A total of 10 recorders were deployed on the Arroux river [figure 3.7]. The precise location of these buoys was determined using a Trimble® GeoHX GPS (manufacturer's accuracy: decimetre). Thus, being visible on aerial photos and IR images, the buoys could be used for the next step in georeferencing.

Figure (3.6) Buoys with thermometers system
Marteau Baptiste © September 05 2018

The measurements generated by the thermometers did not require any correction or special processing. These sensors recorded the temperature at the water surface (up to 10 cm deep) at time steps of one minute, which systematically covered the flight period. The final temperature is the average of the temperatures taken during the flight.

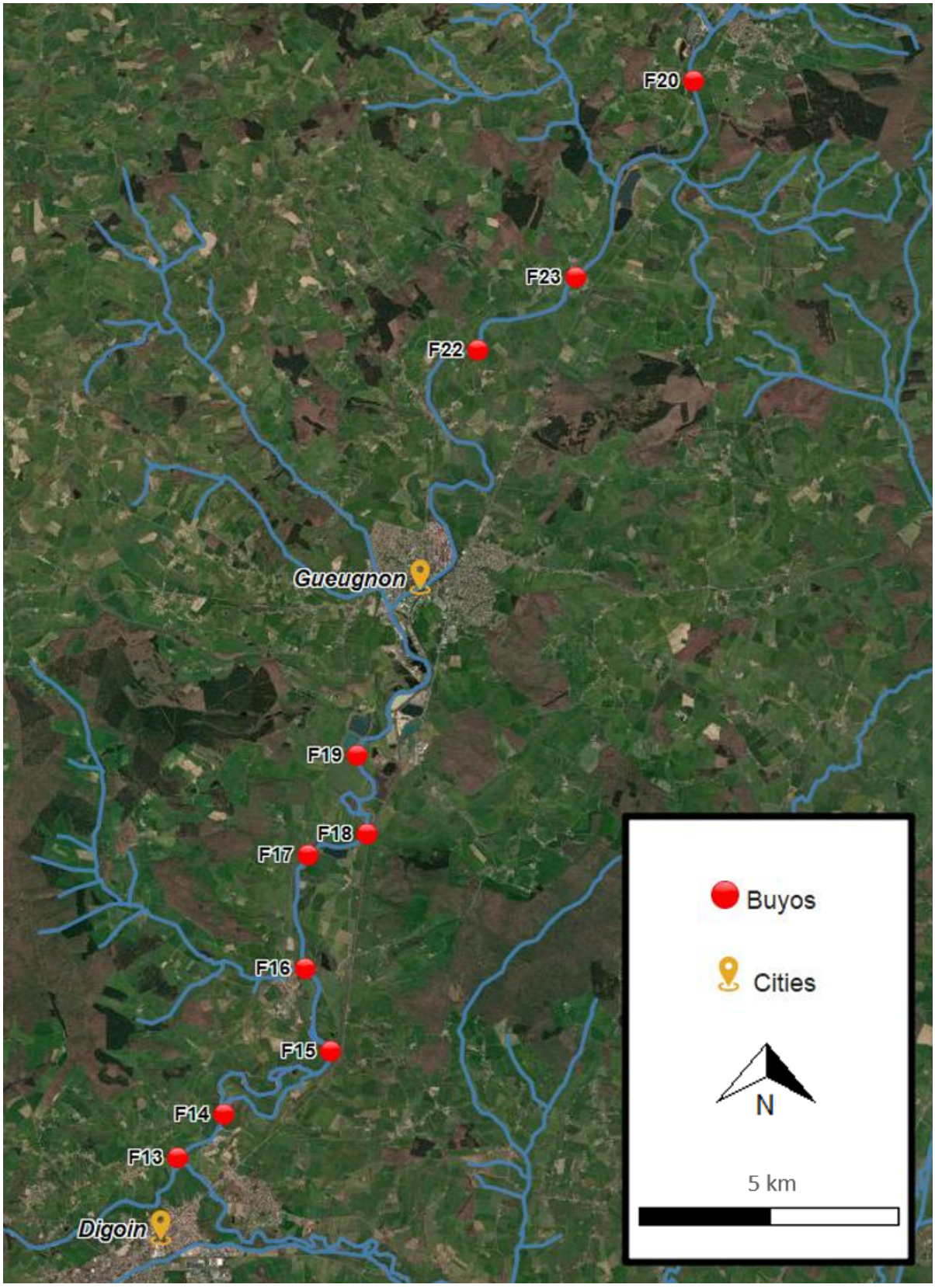

Figure (3.7) Localisation of Buoys in the river

3.3 Data processing

3.3.1 Thermal images to Mosaic IRT

Each sensor recorded a large number of images in order to fly over and cover the study area [figure 3.1]. The orthomosaics were generated by photogrammetry which consists in obtaining reliable measurements from images. Orthomosaic comprises two terms, "ortho" meaning that firstly the images will be orthorectified. The orthorectification aligns the images by geometric corrections to remove distortion, such that each pixel of those images are viewed from directly above. The second term "mosaic" simply means that the ortho-images will be assembled with each other to form a single large, high-resolution image. To carry out these steps, several elements are essential such as the presence of ground control points (GCP) whose geolocation is precisely known (here: buoys) in order to locate the images. In addition a certain percentage of overlap between the images is required to determine common points used by the algorithm to assemble the different images into a single one. The reconstruction was carried out via Agisoft PhotoScan Professional software and provided by Blandine Georges. Information on the data recorded for each sensor is available in the following table [3.1] . We can notice that the number of acquired images is always higher than the number of aligned images because the software selects the photos it will use. For example, if there are too many photos for the same area, or if it does not find a match between the photos, the software will not use them.

Table (3.1) Technical characteristics of data acquisition

		RGB (VISIBLE)	FLIR (IRT)	VarioCAM (IRT)
Nb images acquired	-	1161	1315	1264
Nb images aligned	-	1115	974	1119
Resolution	cm/px	10 and 20	54.5	54.5

The resolution corresponds to the final ground resolution of the reconstructed mosaics.

From fligths, images of the outward and return were taken by the sensors. Therefore, two sets of images, corresponding to the outward and return flights were obtained for both sensors. For part of the results, those two series of images were analysed separately in order to highlight the potential differences between outward and return flights. In addition, the orthomosaic of the combined outward and return flights was also generated via the set of images. To summarize, three orthomosaics are available for each TIR sensor, making six cases :

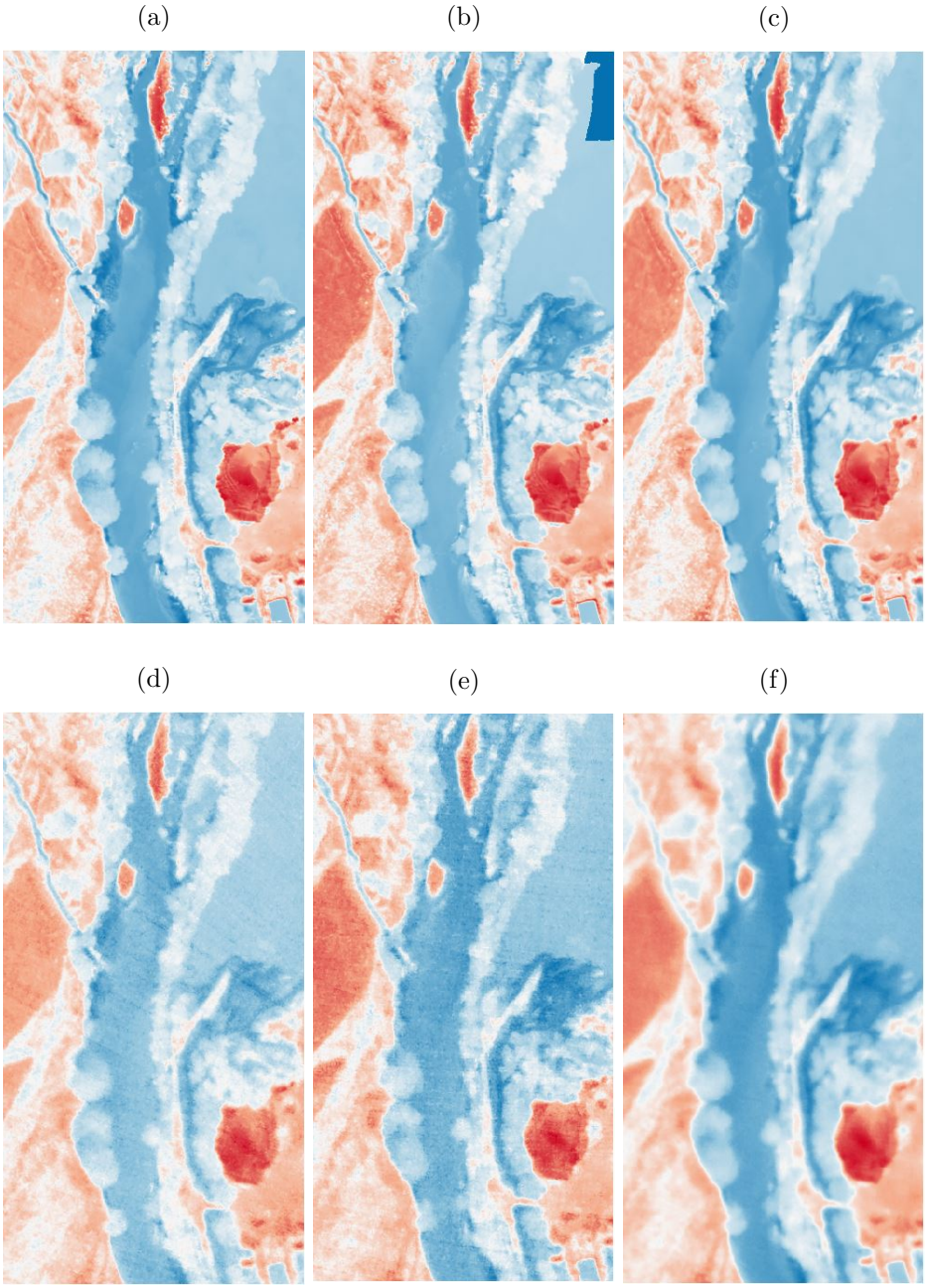

Figure (3.8) Mosaics IRT generated for each cases
(a)VarioCAM® outward flight; (b) VarioCAM® return flight; (c) VarioCAM® outward and return flight (d); FLIR outward flight; (e) FLIR return flight; (f) FLIR outward and return flight / Color gradient: blue for cold temperatures to red for warm temperatures

3.3.2 Correction model for IRT measurement

In this study, the temperatures from recorded IRT measurements are higher than temperatures taken at the buoys. This tendency to overestimate temperature is a common phenomenon observed in the literature (Torgersen et al., 2001; Handcock et al., 2006). Several methods exist to correct the IRT temperatures. However, it depends on the objectives and the equipment available for the experiment. In this study, it was chosen to correct the differences between IRT temperatures and "in-situ" temperatures by applying a linear regression model (Maus et al., 2001). The temperature taken "*in-situ*" by the thermometers will be considered as the real water temperature. .

The IRT temperature was estimated as the average of the pixels surrounding the recorders (8 pixels). To do this, a ring was created using the Qgis software around the location of the buoys. This ring is the result of a difference of two buffers created around the buoys, the larger one with a radius of 1 meter and the smaller one with a radius of 50 centimeters. This surface allows to measure the IRT temperature of the water and not the temperature of the buoy surface (certainly much warmer at this period of the year).

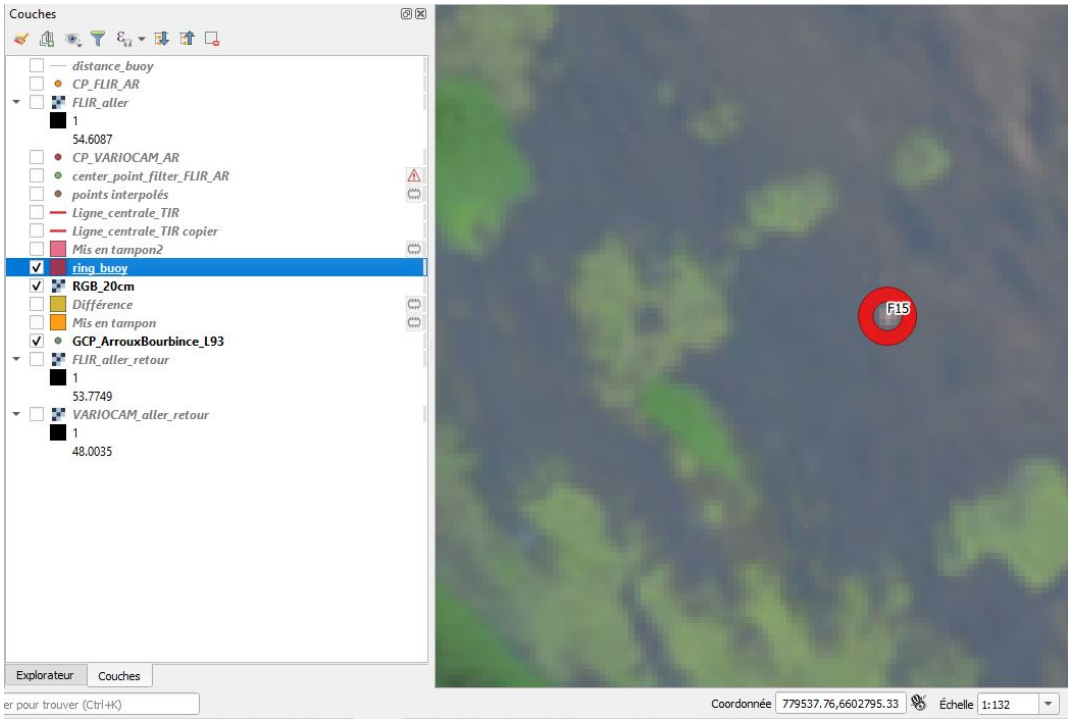

Figure (3.9) Buffer ring around buoy

Once this ring shape has been created, this shapefile is opened via R software. The extraction of the IRT raster is done with the "extract" function of the raster package. The option "FUN = Mean" has been chosen to get an average IRT temperature of the extracted area. Indeed, each pixel of the ring buffer area reflects a temperature data. The purpose of this operation is to have a IRT temperature as representative as possible of this area. The result gives a value of the IRT temperature for each buoy that can be compared to the "in-situ" temperatures taken by the thermometers. A linear regression is then carried out via R in order to show a model linking the IRT temperature and the in-situ temperature. This operation was carried out six times for each case presented in section 3.3.1.

3.3.3 Bland-Altman diagram

In order to assess the agreement between IRT and thermometer, a Bland-Altman test was performed allowing to compare the 2 methods of measurement. Bland-Altman will make it possible to visualize whether the two measurement methods are identical. (Giavarina, 2015). To generate this diagram, the average and the difference between the IRT and the thermometer measurements were calculated. Those values were subsequently plotted on a system of axes, with the x and y axis representing the average and the difference respectively. This process was carried out using the R software with the function "bland.altman.plot" of "BlandAltmanLeh" packages.

3.3.4 Longitudinal temperature profile of the river

The longitudinal temperature profile is one of the most widely used analysis method to highlight spatial variability along the river (Cristea and Burges, 2009; Dugdale, 2016; Maus et al., 2001; Wawrzyniak et al., 2012).

To generate these profiles, a line was drawn using the Qgis software. This line is intended to represent the centre of the watercourse and was drawn by hand along the 35 km using a IRT mosaic as a background map [3.10]. The purpose of drawing it on the IRT mosaic is to extract only the temperature values from pixels representing water. During this step, the central line was drawn through the buoys, allowing to calculate their distance from upstream (vector tool: add attributes of a geometry).

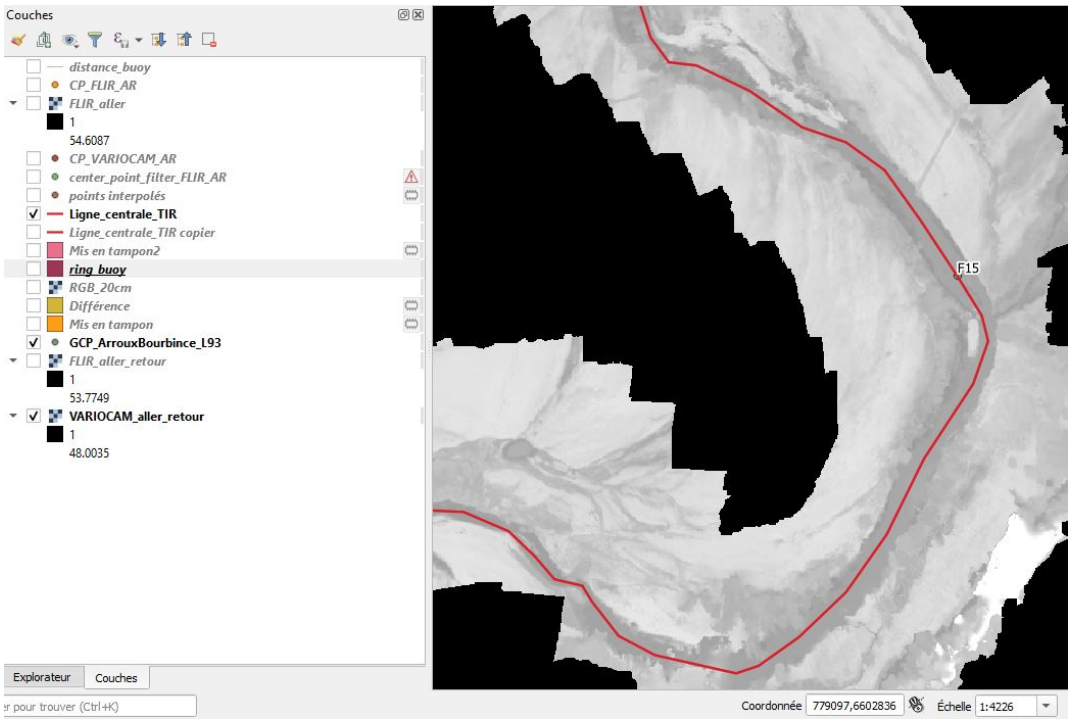

Figure (3.10) Center line of Arroux river

The next step is to generate points along this central line with the same distance each time. For this study a distance of 1 meter was chosen, depending on the resolution of the sensors. Indeed, choosing a distance lower than the resolution of the sensors lead to the extraction of twice the value of the same pixel, which is useless and increases the calculation time. The generation of points allows also to easily select the zones where an obstacle was inevitable (like a bridge) and to assign them [3.11]. This step avoids once

again to extract values of a surface other than water and thus removes outliers from the final graph. The set of points generated on the central line was made twice for each sensor (FLIR and VARIOCAM) because the mosaic was different.

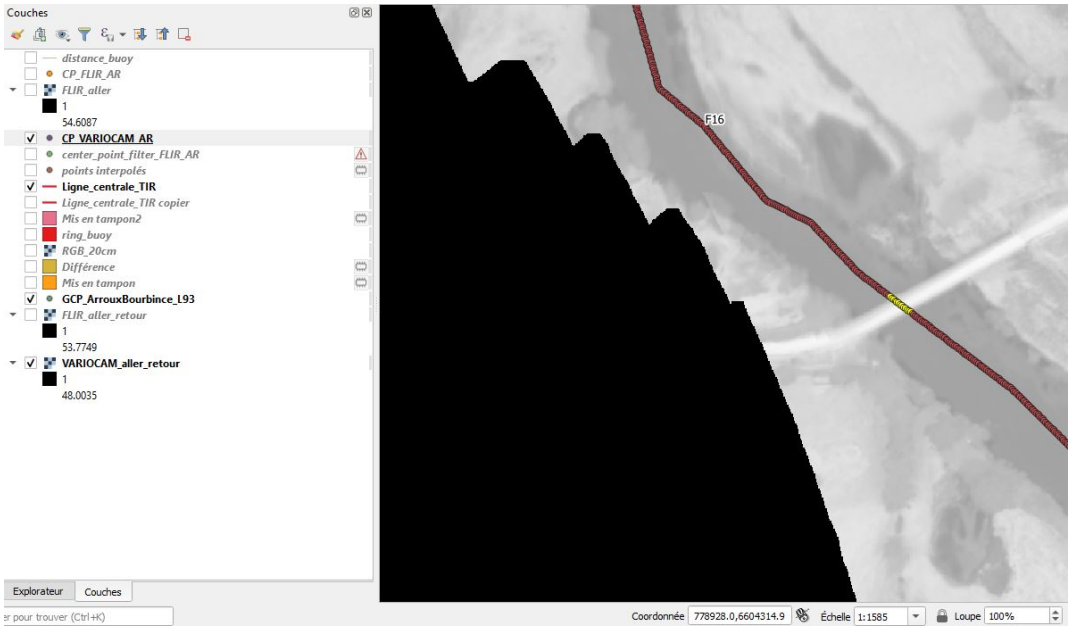

Figure (3.11) Generated points and selection of obstacle

The IRT temperature was extracted in the same way as for the ring buffers of the buoys. The option "FUN = MEAN" was also chosen for the same reasons. Here the extract function was used with the option "BUFFER = 1" in order to take the temperature of each zone of 1 m of diameter around the points and to cover a representative area of the watercourse center. The extract function keeps the attributes of each point and consequently the information "water" or "out of water". The ID of the points enables to add a notion of distance from the upstream as the distance between the points has been fixed. Indeed the distance from the upstream is equal to the ID of the point multiplied by the distance between each point.

Those IRT temperatures are converted by the model created in Section 3.3.2. Then a moving median with a window of 20 is used to smooth the curve (Cristea and Burges, 2009). The R-code for this treatment is available in the Appendix (see section A.3). To summarize, a profile was created for each of the cases presented in section 3.3.1.

3.3.5 Thermal imaging analyses

To analyse the thermal heterogeneities inside the Arroux river, a comparison between RGB rasters and IRT rasters of different zones was conducted. These zones were chosen according to the thermal longitudinal profile of the river (see result 4.3), the specific morphological features of the stream and the human/natural structures surrounding the river. Indeed, the first and second selected zones correspond to high and low temperatures of the thermal profiles, respectively. In addition, the first zone displays the junction between the Arroux and Bourbince rivers while the second one is situated in an urbanized area. Regarding the third zone, it outlines an opposite trend between the two sensors on thermal profiles, the Variocam presenting high temperature values and the FLIR low temperature values . The rasters for those three distinct zones were generated using Qgis by clipping extends corresponding to these areas. This operation created small rasters that were thereafter processed with R software.

From the R software, the different layers of each raster were stacked using the stack function. The raster layers obtained for the VARIOCAM and the FLIR were subsequently corrected based on the linear regression (see results 4.1). Since the raster layers of those two sensors were not restricted to water areas, values above the maximum temperature and below the minimum temperature of the corresponding thermal profile were discorded using clamp function. This operation allowed to remove most of the temperature values not related to the water river. An additional raster, corresponding to the difference between the VARIOCAM and the FLIR processed rasters, was also generated to highlight the variability between the two sensors. This computer manipulation was performed after the FLIR raster was projected on that of the VARIOCAM to get the same extend and resolution. Finally, the RGB, VARIOCAM, FLIR and VAROCAM - FLIR rasters were plotted independently for each zone of study using the ggRGB and ggR functions. Finally, histograms representing the frequency of pixels in function of the temperature values were generated for the VARIOCAM and the FLIR processed rasters using the hist function. All the R codes for each processing are available in the appendix section A.

Chapter 4

Results

4.1 Correction model for IRT measurements

The first important part of the data processing consisted in correcting the IRT measurements to remove atmospheric distortion (Dugdale et al., 2019), see section 1.5.4. To this end, linear regression models using the IRT temperature as a function of the real temperature recorded by the thermometers were generated [figure 4.1]. In those models, each letter corresponds to the different mosaics presented in section 3.3.1.

The linear regression models are used to verify if there is a relationship between the temperature from the IRT remote sensing and the temperature taken by the thermometers on the buoys. Regarding the VARIOCAM sensor, it can be observed that the p-values respond significantly, which means that the model can be assimilated to a linear equation [table 4.1]. At the opposite, the FLIR linear models are not significative which imply that the linear relationship cannot be confirmed. Another important parameter is the determination coefficient (R^2), that assesses the fit of the model. The examination of R^2 indicates that the VARIOCAM data fit better to the models than the FLIR, as the determination coefficient is closer to 1.

In the context of this study, the models generated for the outward and return flight should be more relevant considering that it is a combination of both flights. In fact a higher number of images and points is provided by the outward and return flight,thereby enabling the creation of an orthomosaic more representative of the reality. This has been observed for the VARIOCAM but not for the FLIR.

(a) FLIR outward flight

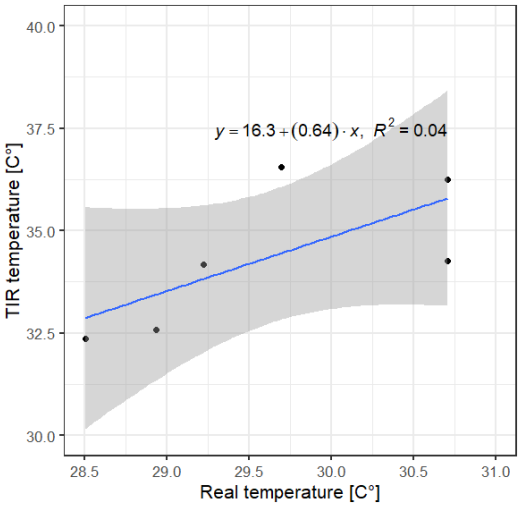

(b) VARIOCAM outward flight

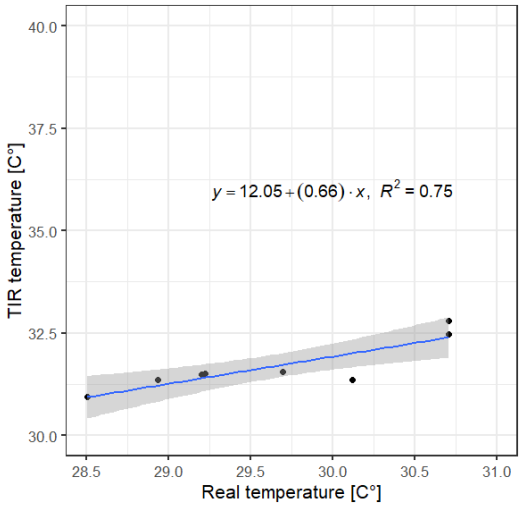

(c) FLIR return flight

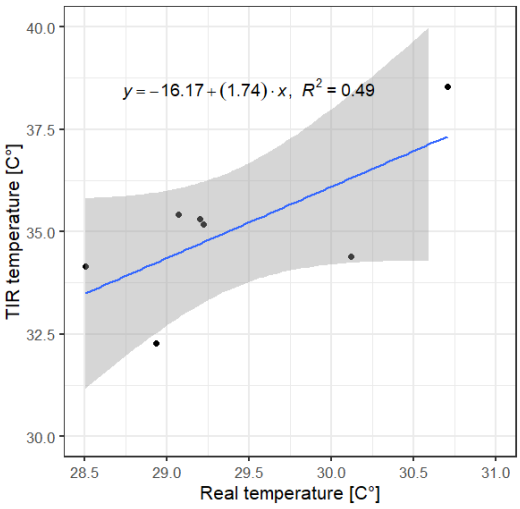

(d) VARIOCAM return flight

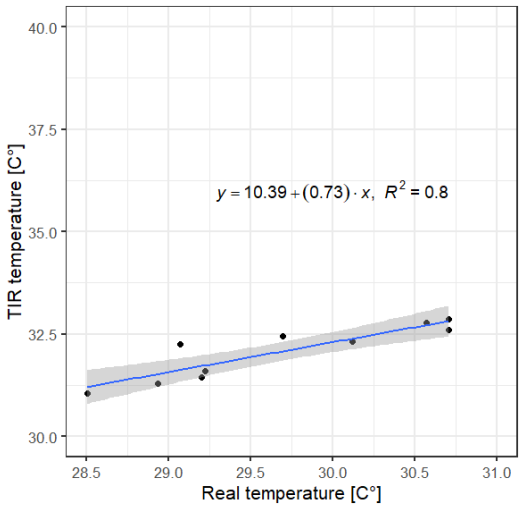

(e) FLIR outward and return flight

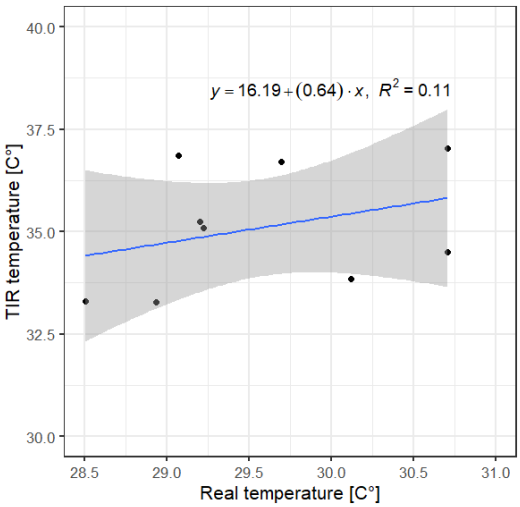

(f) VARIOCAM outward and return flight

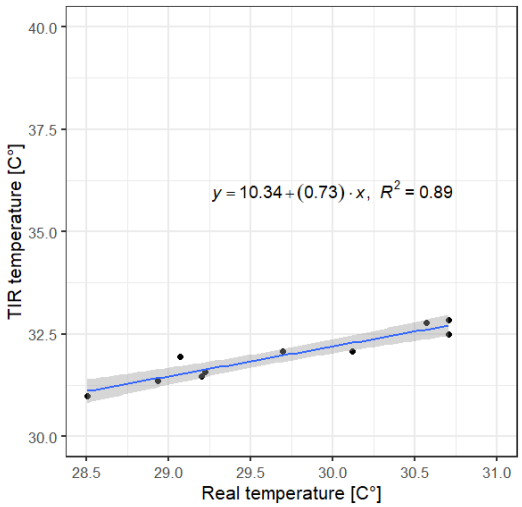

Figure (4.1) Linear regression models
blue : regression line / grey zone : confidence interval (CI) for the slope

Table (4.1) Parameters of linear regression models

Ortho-mosaic	DF	p-value	R^2	RMSE
FLIR outward flight	5	0.6592	0.042	2.895
FLIR return flight	5	0.0882	0.488	1.477
FLIR outward and return flight	7	0.3765	0.113	1.506
VARIOCAM outward flight	6	0.00514*	0.754	0.333
VARIOCAM return flight	8	0.00044**	0.803	0.309
VARIOCAM outward and return flight	8	0.00003***	0.894	0.214

The [table 4.1] presents important parameters for each regression. The RMSE (Root Mean Squared Error) shows that the models for the FLIR deviate on average more strongly than those for VARIOCAM. This means that the difference between the values predicted by the model and the real values are greater. This is confirmed by the observation of R^2 [figure 4.1]. However, some of these interpretations cannot be asserted because not all testing assumptions could be confirmed due to lack of data. In fact, it can be noted that there are only 10 points or fewer per model (see DF : Table 4.1), which does not allow to perform the normality test of the residues. All the results for linear regression are available in the appendix [B.1]. In other words, the empirical function (linear regression) found can be used to predict VARIOCAM measurements but not for FLIR. The relationship found for the FLIR will only be used to correct IRT measurements without quantitative information.

The Figure [4.2] shows the temperature differences between IRT and thermometer measurments at each buoys. From this graph, it can be seen that the temperature difference is comprised between 3 and 11 °C for the FLIR and between 1 and 3 °C for the VARIOCAM. This indicates that both sensors tend to overestimate the water temperature with a stronger effect for the FLIR. These results of overestimation are consistent with the studies conducted by Torgersen et al and Handcock et al (Torgersen et al., 2001; Handcock et al., 2006). In addition, the observation of this figure shows that the temperature differences for the FLIR are more dispersed, suggesting that the camera did not have the same behaviour between the outward and return flight.

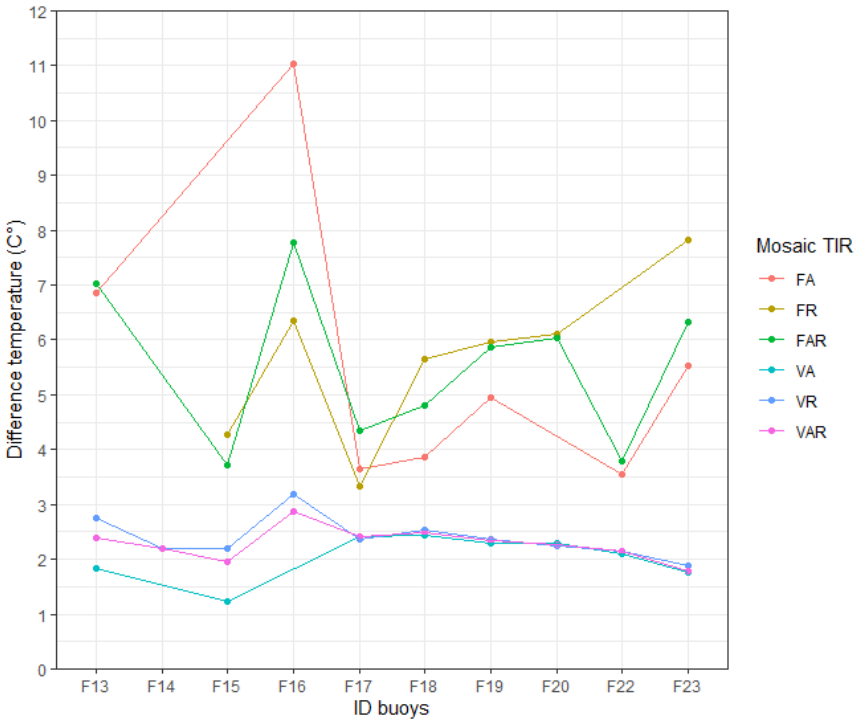

Figure (4.2) Difference of temperature between IRT measurement and thermometer
FA = FLIR outward flight ; FR = FLIR return flight ; FAR = FLIR outward and return flight ; VA = VARIOCAM outward flight ; VR = VARIOCAM return flight ; VAR = VARIOCAM outward and return flight

For the following results [section 4.2/4.3/4.4], it has been chosen to present only the results of outward and return flight. Indeed, these mosaic has the highest completeness and consequently allows the comparison between the two sensors.

4.2 Bland-Altman

In order to evaluate the agreement between two methods of measure, Bland-Altman diagrams have been generated. Indeed, the parameters obtained for the linear regressions in the previous section indicated the degree of relationship between two variables, but did not allow their comparison (Giavarina, 2015). Those diagrams will therefore be used to highlight the comparison between the two methods : IRT remote sensing versus "*in-situ*" thermometer. Diagrams are available below figure [4.3].

(a) FLIR outward and return flight (b) VARIOCAM outward and return flight

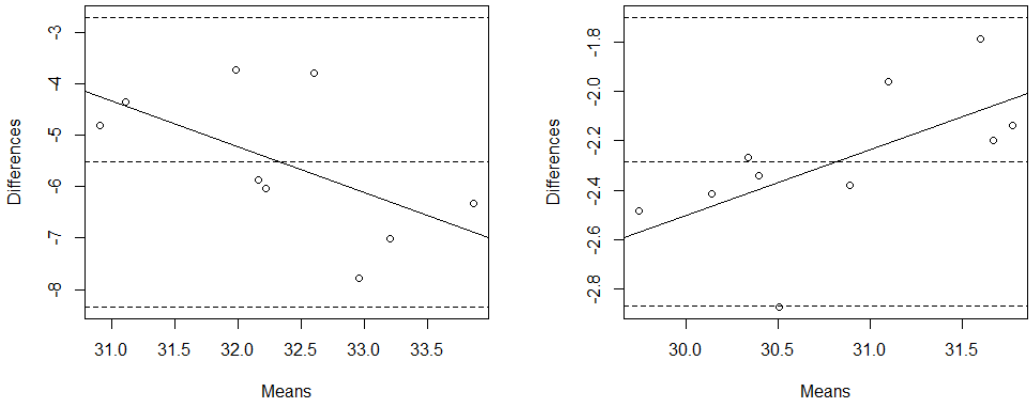

Figure (4.3) Bland and Altman diagrams between *in-situ* thermometer and IRT measurement for each sensor
Abscissa axis : Average of IRT and Thermometer temperature at each buoy.
Ordinate axis : Difference between Thermometer and IRT temperature at each buoy.

These graphs make it possible to confirm in both cases that the IRT measurements overestimate the temperature measured by the thermometers. Indeed, the difference ("in-situ" temperature - IRT temperature) is always negative, and leads to a bias. This confirms the analysis presented in the figure [4.2]. The bias is about 2 C° negative for the VARIOCAM measurements and 5 C° negative for the FLIR. It can also be noticed that this bias is not constant since there is an increment. For the VARIOCAM, the bias decreases as the temperature increases, and this can be confirmed by examining the p-value of the slope of the straight line [Appendix B.2]. The rejection of the null hypothesis, systematic bias inversely proportional, implies that the magnitude of the bias decreases as the temperature increases. For the FLIR nothing can be concluded due to the fact that the linear regression is not significant.

4.3 Longitudinal temperature profile

The longitudinal temperature profile measured by IRT gives a great continuous representation of the spatial variability of the Arroux river for the study area. As mentioned in section 3.3.4, the profiles have been corrected with their regressions presented in figure [4.1]. The IRT derived longitudinal profiles of each sensors (VARIOCAM and FLIR) for outward and return flight are presented in figure [4.4]. As a reminder, the data were collected on July 24, 2019 at 4 pm, with an air temperature close to 38 C°. These dry conditions result in a particularly high water temperature of around 30 C°.

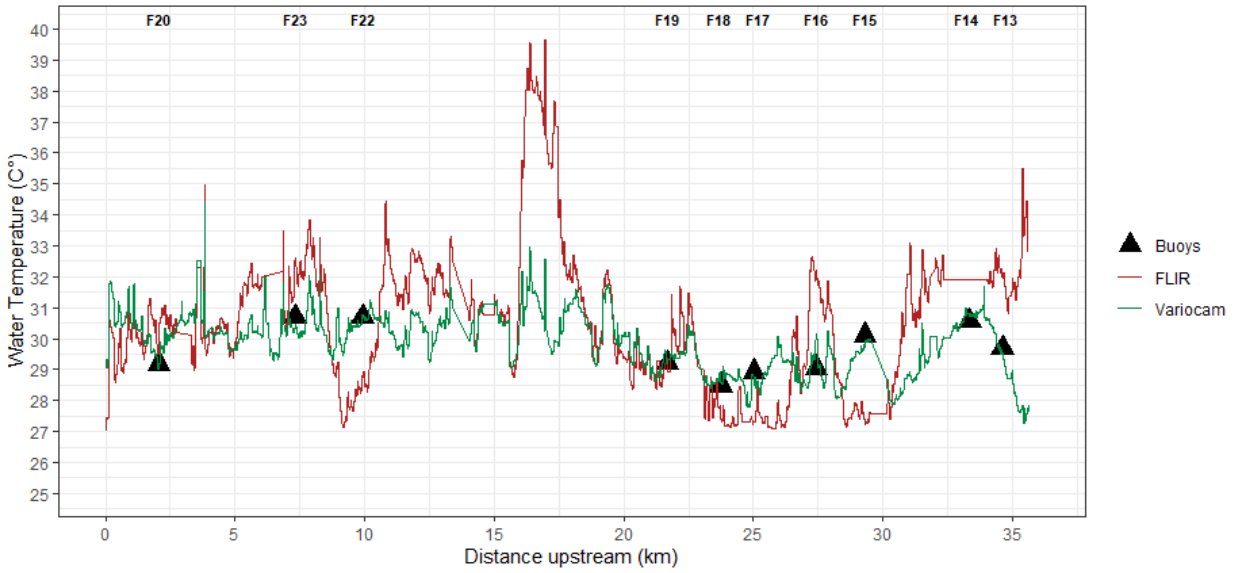

Figure (4.4) Longitudinal temperature profiles for each sensor's outward and return flight
The colour curves represent the longitudinal temperature profile for each IRT sensor generated from a moving average with a window of 50 points (i.e. 50 m). And the black triangles represent the temperature taken "in-situ" at the buoys and assimilated to the real water temperature.

Figure [4.4] shows a significant difference between the VARIOCAM and FLIR profiles. The two IRT sensors do not measure the same temperature even after the regression correction.[4.1]. The VARIOCAM profile is well adjusted to the temperature of the buoys, which is quite logical given the parameters of the linear regression model [table 4.1]. On the contrary, the FLIR does not follow the trend of the VARIOCAM and moreover does not approach the temperature of the buoys. This can be explained by the previous analyses. Indeed the FLIR model was less well adjusted with a higher bias. The result of this is illustrated by the large differences between the curve on the graph. However, sometimes the FLIR seems to behave like the VARIOCAM at kilometer 22.5 for example.

Dishes are interpolations created by the algorithm when values were missing. These dishes are more present for the FLIR because the mosaic was less complete. This feature is observed between km 30 and 35 at buoy 14 [4.4].

Longitudinal profile in the study stream reveals pattern of spatial variability of water temperature. Examination of the variocam curve allows to define maxima and minima along the Arroux study area (35 and 27 C° respectively). In general, a temperature variation between 28 C° and 32 C° is observed. The confidence interval for IRT VARIOCAM profile is equal to the value +/- 0.5 C° , based on the RMSE of the regression [table 4.1] and this interval is similar to what can be found in other studies (Torgersen et al., 2001; Handcock et al., 2012). Due to the poor fit of the FLIR model, the temperature cannot be predicted. In fact, for the FLIR, the correction has been applied and the profile generated just for comparison. The wrong results for the FLIR are certainly due to a failure during the measurement, on the outward or return flight. The profile of the FLIR indicates unusual behavior at the seventeenth kilometer [figure 4.4], with excessively high temperatures. To verify the cause of this abnormal peak, the FLIR ortho-mosaic was analyzed at this location and will be discussed later (section 5).

4.4 Images analysis

The longitudinal temperature profile generated in the previous section highlighted areas with particular thermal behaviour. The analysis of the IRT images at these locations will allow to make assumptions about the causes of these thermal variations. To do this, several treatments have been applied to the ortho-mosaics see section [3.3.1]. Four rasters will be presented on the same figure at the same scale in order to make the comparison easier: an (RGB) aerial photo, the IRT FLIR raster corrected with its linear model, the IRT VARIOCAM raster corrected with its linear model and the difference between the VARIOCAM and the FLIR rasters. Overall, three areas were selected because they show thermal variability at the longitudinal profile scale and have spatial thermal heterogeneities within the same image. In addition, pixel temperature histograms were generated for each camera to observe the temperature distribution for each IRT raster. Again, all the images are from the same flight on July 24 2019 between 4:00 pm and 5:00 pm.

4.4.1 Bourbince tributary zone

This zone was chosen for two reasons. The first one is that it is the affluence zone between the Arroux and the Bourbince (the lateral watercourse on the right side of the image). Secondly, if we look at the graph representing the temperature profile, we can notice a significant decrease in temperature for both sensors. Figure [4.5 (a)] shows where the Bourbince flows into the Arroux and includes the last buoy with ID F13. The real mean temperature of the Bourbince is known from a thermometer placed a little further upstream and is equal to 27.6 C°. The IRT rasters (VARIOCAM and FLIR) show a colder temperature for the Bourbince, which even has a cooling effect on the Arroux. This is confirmed by the temperatures of the two thermometers. One can also notice that the VARIOCAM indicates temperature values close to those of thermometers, which is in adequacy with the previous results. At the upper right hand side of the images figure [4.5] there are colder areas located on the edge of the watercourse. These areas are green on the RGB raster and appear to correspond to aquatic vegetation. This thermal heterogeneity feature will be observed on all images of each different selected zone. Despite the fact that FLIR overestimates the temperature, we can see that it shows the same cold water areas as VARIOCAM. Indeed, even if the temperature is different, the trend remains the same. It can also be highlighted that the difference between the two IRT cameras is approximately constant on the water surface figure [4.5 (d)].

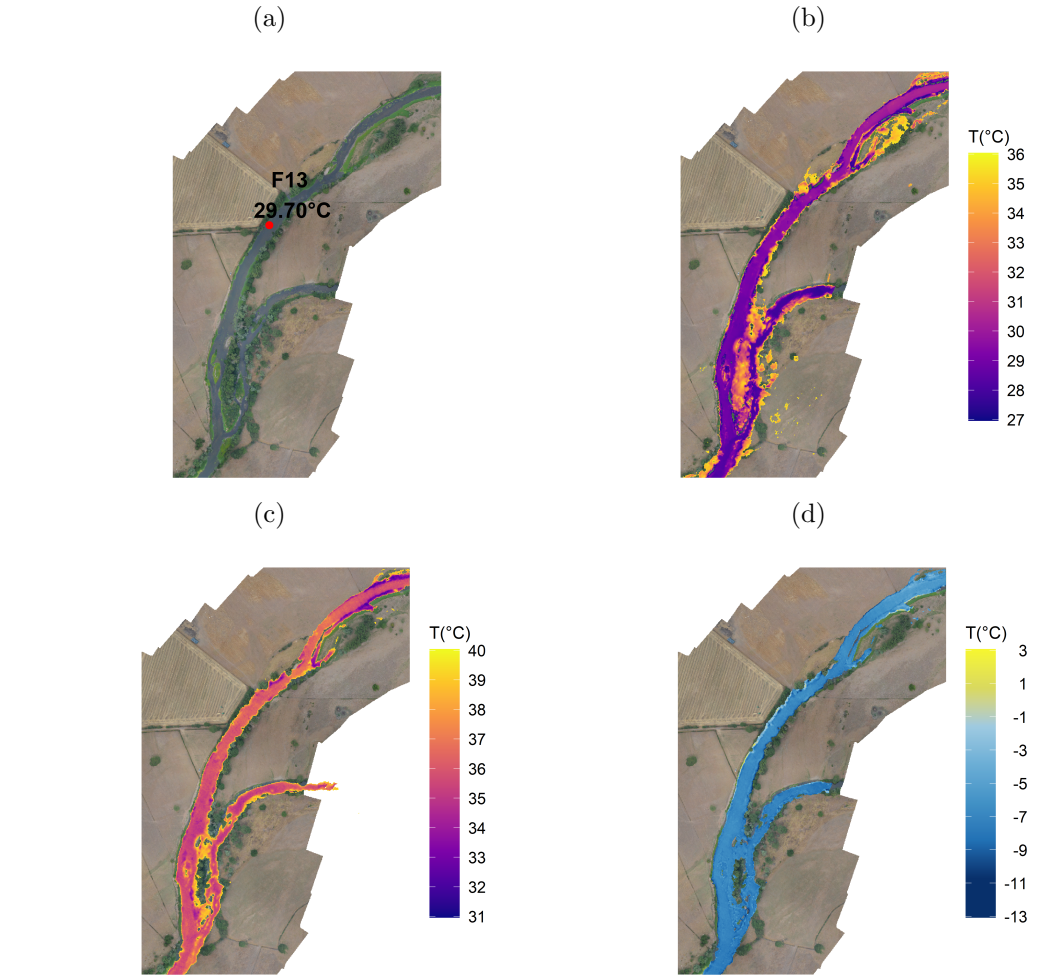

Figure (4.5) Raster comparison : Bourbince tributary zone
(a) Visible (RGB) and temperature at buoys F13 ; (b) VARIOCAM IRT; (c) FLIR IRT; (d) Difference IRT : VARIOCAM - FLIR

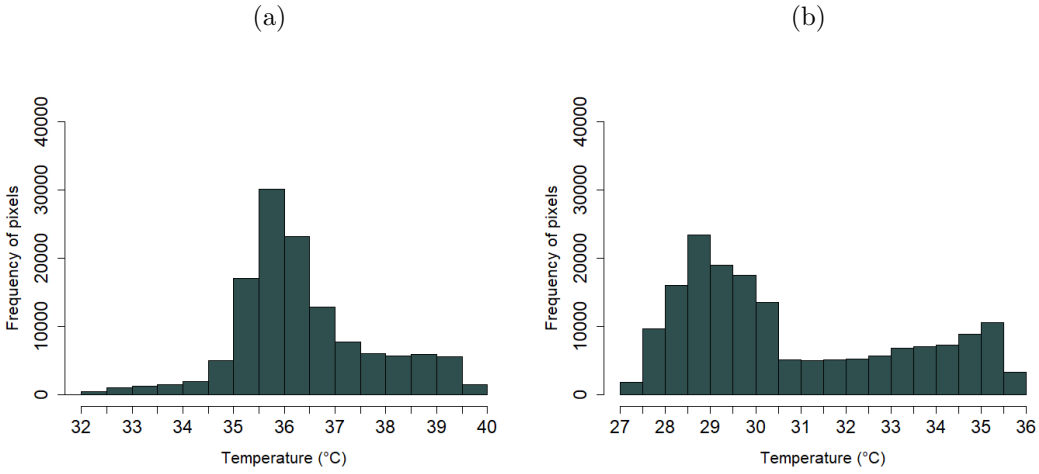

Figure (4.6) Temperature pixel histogram : Bourbince tributary zone
(a) FLIR; (b) VARIOCAM

The temperature pixel histogram from the stream indicates the water temperature distribution for the area under consideration (Cristea and Burges, 2009). From this graph, it can be seen that the mode value is different for the two sensors : 35.5 C° for the FLIR and 28.5 C° for the VARIOCAM. The temperature of 28.5 C° is the most representative value of the zone, as it is closer to that of the thermometer.

4.4.2 Urbanized area: Gueugnon bridge

This zone is located at 17.8 km far from the temperature profile of the Arroux [4.4] and corresponds to a warmer zone figure [4.7]. It can also be observed that the land use is urbanized, with the presence of a bridge and buildings. From these images, we can firstly notice that the aquatic vegetation creates a colder area near the bridge and therefore confirms the trend observed in the figure [4.5]. In addition, if we follow the movement of the water from upstream to downstream, we can see on VARIOCAM IRT raster that the water temperature has a tendency to warm up. The opposite trend can be observed for the FLIR IRT raster. Finally, the water around the islets is much warmer regarding both IRT rasters. Once again, the FLIR, despite the fact that it gives an erroneous temperature measurement, highlights the same areas of thermal variability.

Concerning the temperature pixel histogram [4.8], it can be observed the pixel distribution mode is much warmer than in the previous case: 36.5 C° for the FLIR and 31 C° for the VARIOCAM which confirms that the measured IRT temperatures are warmer. Moreover, the temperature distribution is different between the two cameras, which means that the sensors do not react in the same way when taking measurements. This feature is particularly marked on this graph [4.8].

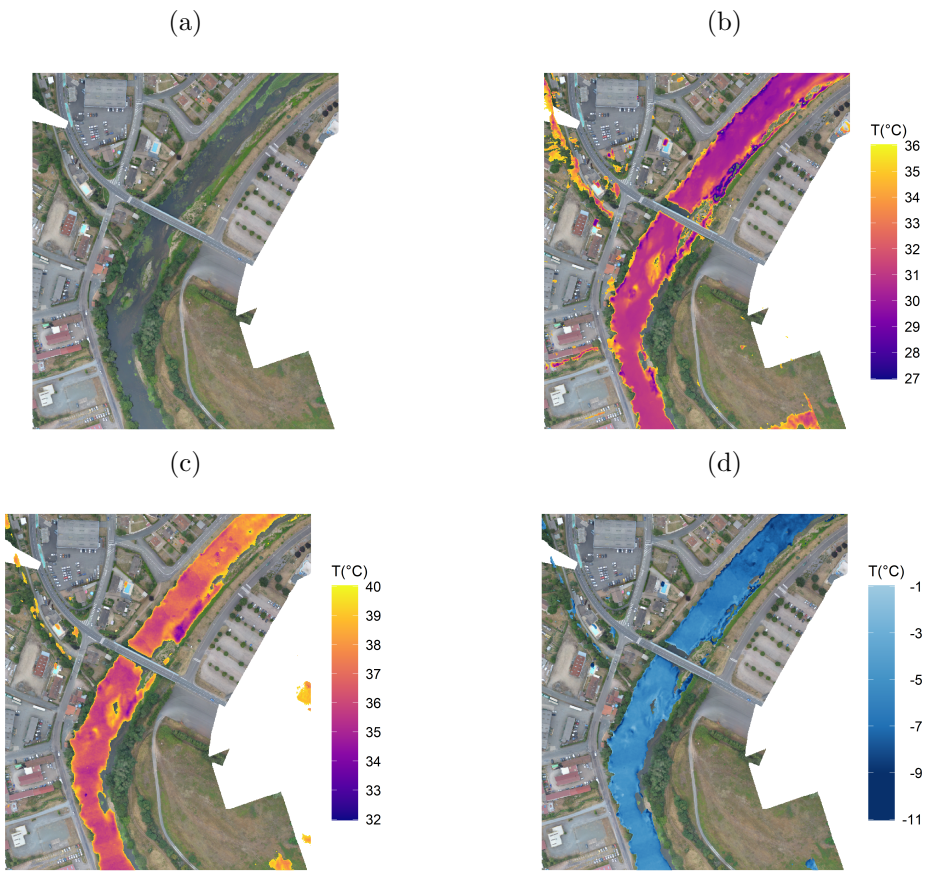

Figure (4.7) Raster comparison : Urbanized area of Gueugnon bridge
(a) Visible (RGB) ; (b) VARIOCAM IRT; (c) FLIR IRT; (d) Difference IRT : VARIOCAM - FLIR

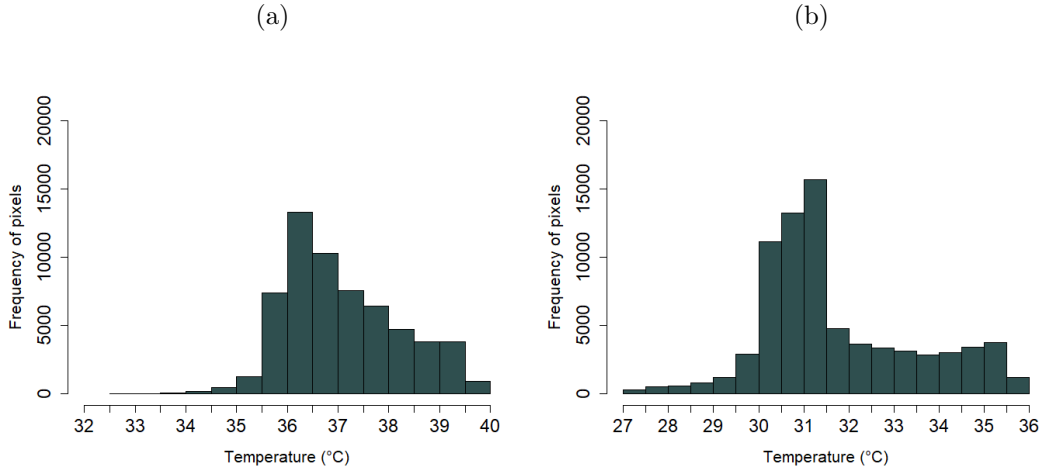

Figure (4.8) Temperature pixel histogram : Urbanized area of Gueugnon bridge
(a) FLIR; (b) VARIOCAM

4.4.3 Buoy F15 area

The following area [4.9] was chosen because the profile trend between the two cameras is the opposite. Indeed, if we refer to the graph of the longitudinal profile [4.4], at buoy F15, we are at the local maximum for the VARIOCAM while the FLIR considers it as a minimum. However, when we look at the thermal variability within the river, it seems to follow the same pattern. Once again we can notice that the aquatic vegetation seems to have the same cooling impact on the water temperature. Lastly, a characteristic feature of IRT remote sensing studies in river environments can be observed and concerns the small tributary streams that are colder (Cristea and Burges, 2009; Dugdale, 2016; Wawrzyniak et al., 2013; Torgersen et al., 2001). The small tributary stream can be seen in the pictures at the bottom right not far from the buoy, but is certainly too small to have a cooling impact on the Arroux.

The temperature distribution [4.10] indicates that the mode for the FLIR is 32 °C and 28.5 C° for the VARIOCAM. It would therefore appear that the FLIR camera has a lower overestimate of water temperature for this area. The temperature at the buoy F15 is 30 C° which is quite far from the distribution mode of the VARIOCAM.

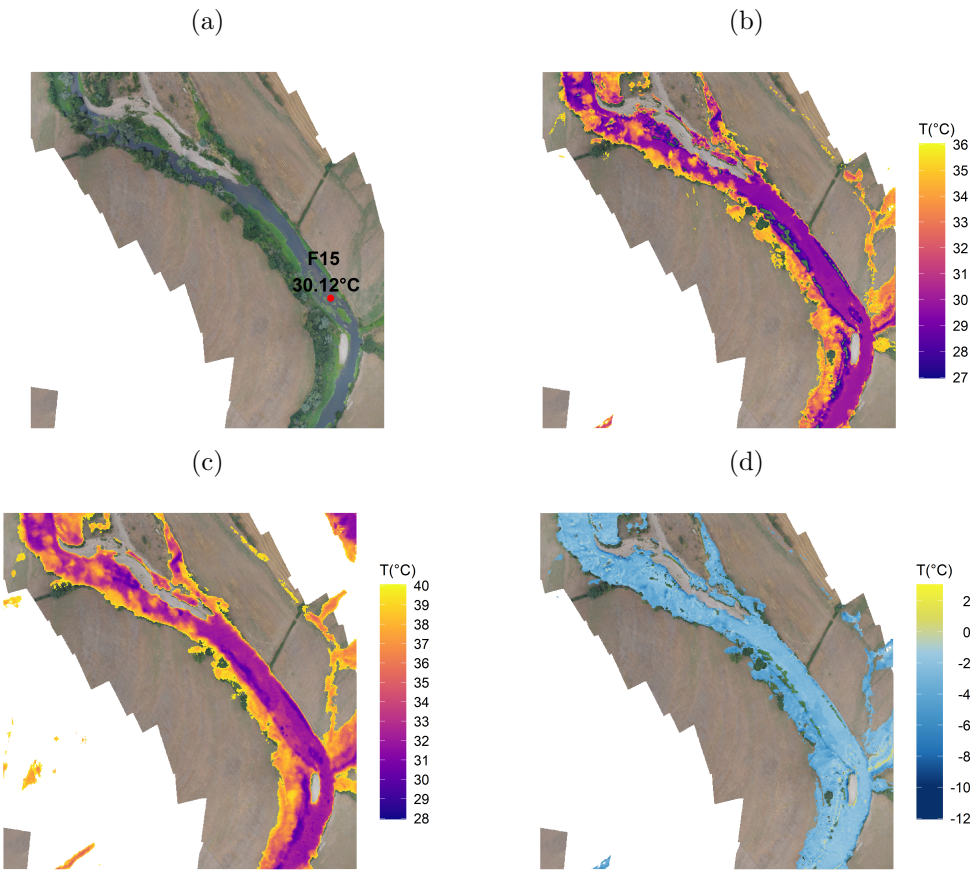

Figure (4.9) Raster comparison : Buoy F15 area
(a) Visible (RGB) and temperature at buoys F15 ; (b) VARIOCAM IRT; (c) FLIR IRT; (d) Difference IRT : VARIOCAM - FLIR

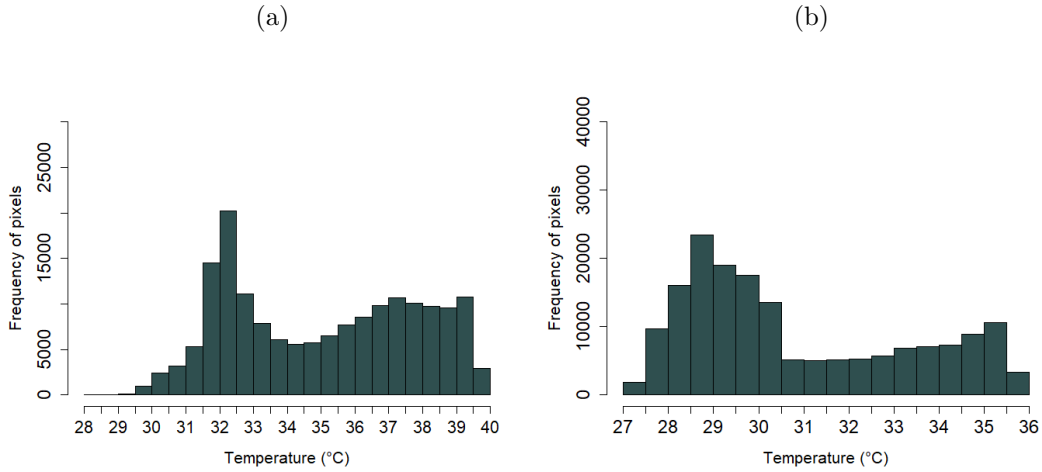

Figure (4.10) Temperature pixel histogram : Buoy F15 area
(a) FLIR; (b) VARIOCAM

Chapter 5

Discussion

The objectives of this work were to compare different temperature measurement methods (IRT remote sensing, *in situ* thermometer) and to use the collected data in order to analyse the spatial temperature variability within a river. For this, several treatments were performed (regression, bland-altman, raster comparison). The results highlighted some differences in the behaviour of the two IRT cameras. Moreover, the raster comparison allowed to identify hot and cold water areas in the stream which could be explained.

5.1 FLIR results

The different results of the FLIR camera are complementary and confirm abnormal behavior when taking measurements [4.1,4.1,4.4]. The camera seems to be working correctly at some point. But from time to time an obvious malfunction appears as shown in the figure [5.1] below. The areas where the FLIR malfunctioned were identified by looking for abnormal trends in the longitudinal temperature profile [4.4]. Indeed, at the 17th kilometre, a temperature peak can be easily observed. The uncorrected orthomosaics of the separate FLIR flights were therefore reviewed to understand the cause of this behaviour. After analysis, effectively, the IRT image of the FLIR return flight reveals some problems during data acquisition.

Figure (5.1) Orthomosaic IRT of the FLIR during the return flight at the 17th km

The temperature measured on the orthomosaic is definitely too high and can be explained by a wrong camera measurement. The darker pixels, closest to red, are the warmest. Temperature drift (inter-image bias), can be the result of many factors or a combination of several factors. It is a common problem encountered in IRT temperature measurement work and is the subject of many studies (Dugdale et al., 2019; Ribeiro-Gomes et al., 2017; Olbrycht and Wiecek, 2015). One of the main causes of the drift of temperature is the heating of the microbolometer. The microbolometer is the part of the sensor that converts radiation into voltage via its electrical resistance. This part of the sensor, when it is not cooled down, is called "uncooled microbolometer". The FLIR camera belongs to those sensors and therefore has a temperature bias when it overheats (Dugdale et al., 2019; Kelly et al., 2019; Handcock et al., 2006). Many factors can influence microbolometer measurement: internal heating of the camera, relative air humidity, topographic shading, time passed during the survey, external radiation,etc (Dugdale et al., 2019).

The FLIR camera overheated while the VARIOCAM worked well, however, there were two uncooled microbolometer thermal cameras. There are differences between the two sensors that could explain this. Firstly, the FLIR are becoming increasingly miniaturized to be mounted on light vehicles such as drones. The ventilation is then lower and the walls of the sensor heat up by radiating the microbolometer (Dugdale et al., 2019). Secondly, the internal components of the two cameras are not the same, which leads to a different behaviour.

Artifacts in the form of lighter and darker bands in red can be seen on this orthomosaic [5.1]. These artifacts are the product of an effect known as the vignetting effect, and are introduced when images are assembled during the creation of orthomosaics (Kelly et al., 2019; Goldman, 2005). The vignetting effect is characterized as a radial falloff of intensity from the center of the image (Goldman, 2005). This effect can create temperature differences of several degrees. Here the main cause is undoubtedly the overheating of the camera causing the temperature drift explained above. however, the causes of the vignetting effect could be multiple, including internal thermal camera parameters such as focal length, or misalignment between sensor and lens,etc but also external patterns such as a bad reception of the incident radiation. Various solutions exist to reduce this effect. One of the simplest is to exclude the edge of the images during the production of orthomosaics and there are many others which are the subject of complete studies (Kelly et al., 2019).

FLIR cameras give results with low accuracy (in comparison with the VARIOCAM) leading to erroneous temperature measurements. However, comparison of the rasters [4.5] showed that the FLIR identified the same warm and cold areas within a section of the stream. When the FLIR camera is not in a warm-up phase it seems to operate in the range indicated by the manufacturer.

5.2 VARIOCAM results

The results of the VARIOCAM camera do not show any abnormalities in the measurement. The sensor worked well, and allows an estimation of the water temperature with +/- 0.5 C° after correction with the linear model. This result is comparable with what can be found in the literature (Torgersen et al., 2001; Handcock et al., 2012; Dugdale, 2016).

5.3 Correction model for IRT measurements

It was necessary to remove the bias in the IRT data caused by atmospheric distortion (Dugdale et al., 2019). Atmospheric distortion is a term to cover errors related to parameters influencing the recording airborne data such as absorption, reflection,... and presented in the introduction of this document (see section 1.5.4). For this purpose a linear regression model was generated with temperature recordings by ground thermometers. The bias can be identified by an altman bland analysis (Giavarina, 2015) and was presented on this graph [4.3]. In order to check if the correction generated by the model has eliminated the bias, a Bland-Altman analysis can be performed again, but this time on the corrected IRT measurements. This verification is available on the following graph [5.2].

(a) FLIR outward and return flight (b) VARIOCAM outward and return flight

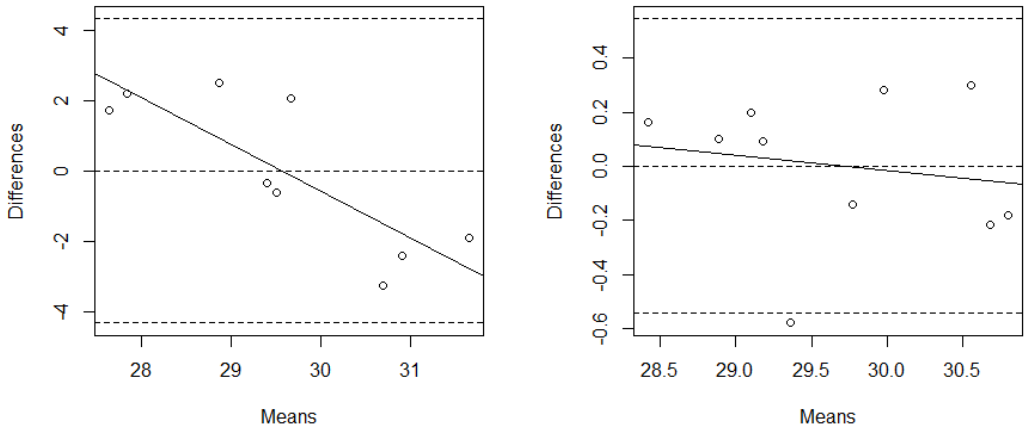

Figure (5.2) Bland and Altman diagrams between *in-situ* thermometer and IRT measurement for each sensors corrected with linear regression model
Abscissa axis : Average of IRT corrected and Thermometer temperature at each buoy.
Ordinate axis : Difference between Thermometer and IRT corrected temperature at each buoy.

Figure [5.2] confirms that the linear model cancels the bias because the trend of the points approaches the horizontal through zero. The results are again poorer for FLIR for the same reasons explained previously. This analysis confirms all the results.

5.4 Identified spatial thermal heterogeneity

The analysis of the IRT images made it possible to identify very distinct areas of thermal variability in the river. For example, the areas of aquatic plants that appear colder on all IRT images [5.3]. These areas of cold water are caused by the development of an invasive plant native to the Americas. *Ludwigia peploides* (Kunth) Raven ssp. and *Ludwigia grandiflora* (Michaux) Greuter and Burdet ssp. are species that spread in the '70s and colonised the Loire basin. Currently, these two *Ludwigia* species continue to expand and are considered a real threat to river biodiversity. It grows particularly fast because it has a clonal reproduction system, a small piece of branch carried away by water can lead to a new plant (Ruaux et al., 2009). The water is colder there because it is a phenomenon of cause and effect. The plant likes calm water with little current. The more the plant develops, the more the water is slowed down by the leaves, and the more the plant tends to develop further. The development of its plants brings a lot of shadow to the water, blocking the sun's radiation from warming it up.

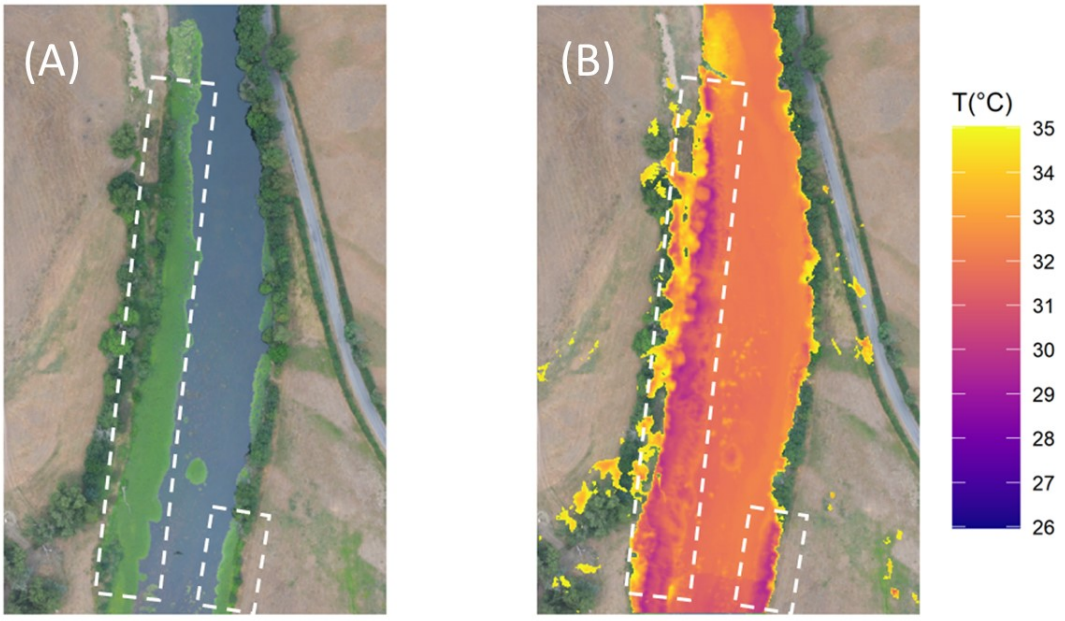

Figure (5.3) Zone of thermal heterogeneity caused by aquatic plant : *Ludwigia*
(A) Visible RGB
(B) VARIOCAM IRT outward and return corrected

Other examples of thermal variability have also been observed, such as colder tributary streams. Thermal cameras therefore make it possible to observe these thermal heterogeneities thanks to their high resolution, which would not have been possible with thermometers alone.

Chapter 6

Perspectives

This work could lead to further researches, including the improvement of the process used in this study and its adaptation to the use of UAVs. Indeed, remote sensing has been booming in recent years thanks to the development of UAVs, miniaturisation and computing power. The use of UAVs allow the repeatability of low-level flights and lower cost than conventional flights (helicopter, plane, etc) for IRT measurements (Lee et al., 2016). Moreover, the low-level flight results in high ground resolution and can reduce atmospheric distortion (Dugdale et al., 2019). The use of the UAV could also enable to fly over narrower rivers because of the manoeuvrability with which it can be piloted.

The FLIR camera has been designed for this kind of application. In fact, its light weight (115 gr) and its small dimensions [44.45mm (h) x 44.45mm (w) x 62.6mm (d)] gives it the capacity to be mounted on a UAV. However, these characteristics lead to the sensor being subject to temperature drift as observed in the section [5.1] of this study. This temperature drift phenomenon represents the main obstacle for the collection of spatial temperature data. Until this problem is resolved, IRT remote sensing by UAV will not be able to be exploited to its full potential (Dugdale et al., 2019).

Several studies propose solutions to reduce the temperature drift but also the bias induced by atmospheric distortion. On one hand, there are calibration protocols for IRT cameras. (Ribeiro-Gomes et al., 2017; Budzier and Gerlach, 2015; Goldman, 2005). And on the other hand, numerous studies are looking for a method to compensate the thermal drift (Olbrycht and Wiecek, 2015; Dugdale et al., 2019). However, these methods are complex and time-consuming and can in some cases be difficult to implement.

An interesting option in line with Dugdale et al (2019) could be investigated in the future. The results of this study indicated that it may be possible to limit the impact of thermal drift. Indeed, flights would have to be conducted during overcast or partly cloudy conditions. This would limit the heating of the camera by external radiation (Dugdale et al., 2019). Then several flights would have to be carried out with the UAV in order to have the maximum number of repetitions (keeping in mind that the atmospheric conditions must remain as constant as possible during the data acquisition). In addition, the speed of flight must be reduced to the lowest in order to limit the rate of image recording (which can heat up the camera (Dugdale et al., 2019)) while keeping a sufficient overlap for the construction of the orthomosaics. A solution to avoid a long and complex calibration or compensation of processing would be to exclude images that show abnormal behaviour (often an overestimation of the temperature which therefore appears as lighter spots on the image). For example, if the UAV performs several outward and return flights to cover the area of interest, only images with acceptable features should be selected for the construction of the final orthomosaic. This will significantly improve the regression model for empirical correction with thermometers and thus lead to a more accurate water temperature value.

Chapter 7

Conclusion

In conclusion, this work made it possible to highlight the measurement differences between temperature sensors. It also proved the complementarity between classical in-situ measurements by thermometers and infrared thermography in a system such as rivers. And finally, the TIR images obtained revealed spatial temperature variability within the river, allowing analysis. This was done without complex or time-consuming sensor calibration, with satisfactory results that were comparable to the literature.

Bibliography

(2012). Climat Paray-le-Monial (France). https://fr.climate-data.org/europe/france/bourgogne/paray-le-monial-8283/. [Online; accessed 26-May-2020].

(2015). Infrared thermography. http://coxcamera.com/technology/infrared-thermography/. [Online; accessed 10-June-2020].

(2017). Caméra thermique et thermographie infrarouge. http://fit-solutions.fr/thermographie-infrarouge/camera-thermique/. [Online; accessed 24-May-2020].

(2019). En quoi consiste la fonctionnalité MSX® ? https://www.flir.fr/discover/professional-tools/what-is-msx/. [Online; accessed 10-June-2020].

Antonopoulos, V. Z. and Gianniou, S. K. (2003). Simulation of water temperature and dissolved oxygen distribution in Lake Vegoritis, Greece. *Ecological Modelling*, 160(1-2):39–53.

Arconada, A., Argiriou, A., Papini, F., and Pasquetti, R. (1987). La Mesure en Thermographie Infrarouge: Calibration et Traitement du Signal. *Journal of Modern Optics*, 34(10):1327–1335.

Atwell, B. H., MacDonald, R. B., and Bartolucci, L. A. (1971). Thermal mapping of streams from airborne radiometric scanning. *Journal of the American Water Resources Association*, 7(2):228–243.

Budzier, H. and Gerlach, G. (2015). Calibration of uncooled thermal infrared cameras. *Journal of Sensors and Sensor Systems*, 4(1):187–197.

Buffington, J. M. and Tonina, D. (2009). Hyporheic Exchange in Mountain Rivers II: Effects of Channel Morphology on Mechanics, Scales, and Rates of Exchange. *Geography Compass*, 3(3):1038–1062.

Caissie, D. (2006). The thermal regime of rivers: a review. *Freshwater Biology*, 51(8):1389–1406.

Caldwell, S., Kelleher, C., Baker, E., and Lautz, L. (2019). Relative information from thermal infrared imagery via unoccupied aerial vehicle informs simulations and spatially-distributed assessments of stream temperature. *Science of The Total Environment*, 661:364–374.

Chang, N.-B., Imen, S., and Vannah, B. (2015). Remote Sensing for Monitoring Surface Water Quality Status and Ecosystem State in Relation to the Nutrient Cycle: A 40-Year Perspective. *Critical Reviews in Environmental Science and Technology*, 45(2):101–166.

Chen, C., Shi, P., and Mao, Q. (2003). Application of Remote Sensing Techniques for Monitoring the Thermal Pollution of Cooling-Water Discharge from Nuclear Power Plant. *Journal of Environmental Science and Health, Part A*, 38(8):1659–1668.

Cherkauer, K. A., Burges, S. J., Handcock, R. N., Kay, J. E., Kampf, S. K., and Gillespie, A. R. (2005). Assessing satellite-based and aircraft-based thermal infrared remote sensing for monitoring pacific northwest river temperature. *Journal of the American Water Resources Association*, 41(5):1149–1159.

Cristea, N. C. and Burges, S. J. (2009). Use of Thermal Infrared Imagery to Complement Monitoring and Modeling of Spatial Stream Temperatures. *Journal of Hydrologic Engineering*, 14(10):1080–1090.

Demba, A., Mohamed, K. M., and Ould, M. O. S. (2013). Contribution a l'étude de la qualité physico-chimique de l'eau de la rive droite. *LARHYSS Journal P-ISSN 1112-3680/E-ISSN 2602-7828*, (12).

Dugdale, S. J. (2016). A practitioner's guide to thermal infrared remote sensing of rivers and streams: recent advances, precautions and considerations: A practitioner's guide to thermal infrared remote sensing of rivers and streams. *Wiley Interdisciplinary Reviews: Water*, 3(2):251–268.

Dugdale, S. J., Bergeron, N. E., and St-Hilaire, A. (2015). Spatial distribution of thermal refuges analysed in relation to riverscape hydromorphology using airborne thermal infrared imagery. *Remote Sensing of Environment*, 160:43–55.

Dugdale, S. J., Kelleher, C. A., Malcolm, I. A., Caldwell, S., and Hannah, D. M. (2019). Assessing the potential of drone-based thermal infrared imagery for quantifying river temperature heterogeneity. *Hydrological Processes*, 33(7):1152–1163.

Durance, I. and Ormerod, S. J. (2007). Climate change effects on upland stream macroinvertebrates over a 25-year period. *Global Change Biology*, 13(5):942–957.

Ebersole, J. L., Liss, W. J., and Frissell, C. A. (2003). Cold water patches in warm streams: physicochemical characteristics and the influence of shading. *Journal of the American Water Resources Association*, 39(2):355–368.

Garrigues, S., Allard, D., Baret, F., and Weiss, M. (2006). Quantifying spatial heterogeneity at the landscape scale using variogram models. *Remote Sensing of Environment*, 103(1):81–96.

Georges, B., Rollin, X., and Michez, A. (2019). Suivi de la température des cours d'eau wallons. Potentiels et contraintes du réseau aqualim. (13).

Giavarina, D. (2015). Understanding Bland Altman analysis. *Biochemia Medica*, 25(2):141–151.

Goldman, D. (2005). Vignette and exposure calibration and compensation. *IEEE transactions on pattern analysis and machine intelligence*, 32(12):899–906.

Hamblin, P. and McAdam, S. (2003). Impoundment effects on the thermal regimes of Kootenay Lake, the Arrow Lakes Reservoir and Upper Columbia River. *Hydrobiologia*, 504(1-3):3–19.

Handcock, R., Gillespie, A., Cherkauer, K., Kay, J., Burges, S., and Kampf, S. (2006). Accuracy and uncertainty of thermal-infrared remote sensing of stream temperatures at multiple spatial scales. *Remote Sensing of Environment*, 100(4):427–440.

Handcock, R. N., Torgersen, C. E., Cherkauer, K. A., Gillespie, A. R., Tockner, K., Faux, R. N., and Tan, J. (2012). Thermal Infrared Remote Sensing of Water Temperature in Riverine Landscapes. In *Fluvial Remote Sensing for Science and Management*, pages 85–113.

Isaak, D. J., Wollrab, S., Horan, D., and Chandler, G. (2012). Climate change effects on stream and river temperatures across the northwest U.S. from 1980–2009 and implications for salmonid fishes. *Climatic Change*, 113(2):499–524.

Jacob-Rousseau, N., Météry, F., Tscheiller, C., and Navratil, O. (2016). La petite hydraulique agricole et industrielle, de l'histoire économique à l'évaluation quantitative des presssions sur les écoulements, XIXe - début XXe siècle. Bassin de l'Arroux, de la Grosne et de la petite Grosne (Bourgogne, France). *BSGLg*.

Johnson, S. L. and Jones, J. A. (2000). Stream temperature responses to forest harvest and debris flows in western Cascades, Oregon. *Canadian Journal of Fisheries and Aquatic Sciences*, 57(S2):30–39.

Jonsson, B. and Jonsson, N. (2018). Egg incubation temperature affects the timing of the Atlantic salmon *Salmo salar* homing migration. *Journal of Fish Biology*, 93(5):1016–1020.

Kay, J. E., Kampf, S. K., Handcock, R. N., Cherkauer, K. A., Gillespie, A. R., and Burges, S. J. (2005). Accuracy of lake and stream temperatures estimated from thermal infrared images. *Journal of the American Water Resources Association*, 41(5):1161–1175.

Kelly, J., Kljun, N., Olsson, P.-O., Mihai, L., Liljeblad, B., Weslien, P., Klemedtsson, L., and Eklundh, L. (2019). Challenges and Best Practices for Deriving Temperature Data from an Uncalibrated UAV Thermal Infrared Camera. *Remote Sensing*, 11(5):567.

Kupren, K., Mamcarz, A., Kucharczyk, D., Prusińska, M., and Krejszeff, S. (2008). Influence of water Temperature on Eggs Incubation Time and Embryonic Development of Fish From Genus *Leuciscus*. *Polish Journal of Natural Science*, 23(2):461–481.

Lackenby, J., Chambers, C., Ernst, I., and Whittington, I. (2007). Effect of water temperature on reproductive development of Benedenia seriolae (Monogenea: Capsalidae) from Seriola lalandi in Australia. *Diseases of Aquatic Organisms*, 74:235–242.

Langan, S., Johnston, L., Donaghy, M., Youngson, A., Hay, D., and Soulsby, C. (2001). Variation in river water temperatures in an upland stream over a 30-year period. *Science of The Total Environment*, 265(1-3):195–207.

Latte, N., Gaucher, P., Bolyn, C., Lejeune, P., and Michez, A. (2020). Upscaling UAS Paradigm to UltraLight Aircrafts: A Low-Cost Multi-Sensors System for Large Scale Aerial Photogrammetry. *Remote Sensing*, 12(8):1265.

Lee, E., Yoon, H., Hyun, S. P., Burnett, W. C., Koh, D.-C., Ha, K., Kim, D.-j., Kim, Y., and Kang, K.-m. (2016). Unmanned aerial vehicles (UAVs)-based thermal infrared (TIR) mapping, a novel approach to assess groundwater discharge into the coastal zone: UAV based TIR mapping. *Limnology and Oceanography: Methods*, 14(11):725–735.

Leibowitz, S. G., Comeleo, R. L., Wigington Jr., P. J., Weaver, C. P., Morefield, P. E., Sproles, E. A., and Ebersole, J. L. (2014). Hydrologic landscape classification evaluates streamflow vulnerability to climate change in Oregon, USA. *Hydrology and Earth System Sciences*, 18(9):3367–3392.

Lundquist, J. D., Cayan, D. R., and Dettinger, M. D. (2003). Meteorology and Hydrology in Yosemite National Park: A Sensor Network Application. *Information Processing in Sensor Networks*, pages 518–528.

Marsh, N., Rutherford, J. C., Bunn, S. E., and Cooperative Research Centre for Catchment Hydrology (2005). *The role of riparian vegetation in controlling stream temperature in a southeast Queensland stream.* CRC for Catchment Hydrology, Monash University, Clayton, Vic. OCLC: 224593964.

Maus, P., Lachowski, H., Torgersen, C. E., Matthew, S. B., and Faux, R. N. (2001). New approaches for monitoring stream temperature:. page 31.

Meola, C. and Carlomagno, G. M. (2009). Infrared thermography of impact-driven thermal effects. *Applied Physics A*, 96(3):759–762.

Miara, A., Vörösmarty, C. J., Macknick, J. E., Tidwell, V. C., Fekete, B., Corsi, F., and Newmark, R. (2018). Thermal pollution impacts on rivers and power supply in the Mississippi River watershed. *Environmental Research Letters*, 13(3):034033.

Moore, R. D., Spittlehouse, D., and Story, A. (2005). Riparian microclimate and stream temperature response to forest harvesting: a review1. *JAWRA Journal of the American Water Resources Association*, 41(4):813–834.

Olbrycht, R. and Wiecek, B. (2015). New approach to thermal drift correction in microbolometer thermal cameras. *Quantitative InfraRed Thermography Journal*, 12(2):184–195.

Palmer, M. A., Lettenmaier, D. P., Poff, N. L., Postel, S. L., Richter, B., and Warner, R. (2009). Climate Change and River Ecosystems: Protection and Adaptation Options. *Environmental Management*, 44(6):1053–1068.

Pautou, G., Piégay, H., and Ruffinoni, C. (2003). Les Forêts riveraines des cours d'eau: écologie, fonctions et gestion. *Forêt privée française*.

Poole, G. C. and Berman, C. H. (2001). An Ecological Perspective on In-Stream Temperature: Natural Heat Dynamics and Mechanisms of Human-CausedThermal Degradation. *Environmental Management*, 27(6):787–802.

Qiu, H., Hamilton, S. K., and Phanikumar, M. S. (2020). Modeling the effects of vegetation on stream temperature dynamics in a large, mixed land cover watershed in the Great Lakes region. *Journal of Hydrology*, 581:124283.

Quilbé, R., Rousseau, A. N., Moquet, J.-S., Trinh, N. B., Dibike, Y., Gachon, P., and Chaumont, D. (2008). Assessing the Effect of Climate Change on River Flow Using General Circulation Models and Hydrological Modelling – Application to the Chaudière River, Québec, Canada. *Canadian Water Resources Journal*, 33(1):73–94.

Ribeiro-Gomes, K., Hernández-López, D., Ortega, J., Ballesteros, R., Poblete, T., and Moreno, M. (2017). Uncooled Thermal Camera Calibration and Optimization of the Photogrammetry Process for UAV Applications in Agriculture. *Sensors*, 17(10):2173.

Roth, T. R., Westhoff, M. C., Huwald, H., Huff, J. A., Rubin, J. F., Barrenetxea, G., Vetterli, M., Parriaux, A., Selker, J. S., and Parlange, M. B. (2010). Stream Temperature Response to Three Riparian Vegetation Scenarios by Use of a Distributed Temperature Validated Model. *Environmental Science & Technology*, 44(6):2072–2078.

Ruaux, B., Greulich, S., Haury, J., and Berton, J.-P. (2009). Sexual reproduction of two alien invasive Ludwigia (Onagraceae) on the middle Loire River, France. *Aquatic Botany*, 90(2):143–148.

Sinokrot, B. A. and Gulliver, J. S. (2000). In-stream flow impact on river water temperatures. *Journal of Hydraulic Research*, 38(5):339–349.

Sinokrot, B. A. and Stefan, H. G. (1993). Stream temperature dynamics: Measurements and modeling. *Water Resources Research*, 29(7):2299–2312.

Smith, W. L., Knuteson, R. O., Revercomb, H. E., Feltz, W., Howell, H. B., Menzel, W. P., Nalli, N. R., Brown, O., Brown, J., Minnett, P., and McKeown, W. (1996). Observations of the infrared radiative properties of the ocean–implications for the measurement of sea surface temperature via satellite remote sensing. *Bulletin of the American Meteorological Society*, 77(1):41–52.

Speakman, J. and Ward, S. (1998). Infrared thermography: principles and applications. *ZOOLOGY-JENA-*, 101:224–232.

Tockner, K., Paetzold, A., Karaus, U., Claret, C., and Zettel, J. (2006). Ecology of Braided Rivers. In Sambrook Smith, G. H., Best, J. L., Bristow, C. S., and Petts, G. E., editors, *Braided Rivers*, pages 339–359. Blackwell Publishing Ltd., Oxford, UK.

Tonina, D. and Buffington, J. M. (2009). Hyporheic Exchange in Mountain Rivers I: Mechanics and Environmental Effects. *Geography Compass*, 3(3):1063–1086.

Torgersen, C. E., Faux, R. N., McIntosh, B. A., Poage, N. J., and Norton, D. J. (2001). Airborne thermal remote sensing for water temperature assessment in rivers and streams. *Remote Sensing of Environment*, 76(3):386–398.

Usamentiaga, R., Venegas, P., Guerediaga, J., Vega, L., Molleda, J., and Bulnes, F. (2014). Infrared Thermography for Temperature Measurement and Non-Destructive Testing. *Sensors*, 14(7):12305–12348.

Wawrzyniak, V., Piégay, H., Allemand, P., Vaudor, L., Goma, R., and Grandjean, P. (2016). Effects of geomorphology and groundwater level on the spatio-temporal variability of riverine cold water patches assessed using thermal infrared (TIR) remote sensing. *Remote Sensing of Environment*, 175:337–348.

Wawrzyniak, V., Piégay, H., Allemand, P., Vaudor, L., and Grandjean, P. (2013). Prediction of water temperature heterogeneity of braided rivers using very high resolution thermal infrared (TIR) images. *International Journal of Remote Sensing*, 34(13):4812–4831.

Wawrzyniak, V., Piégay, H., and Poirel, A. (2012). Longitudinal and temporal thermal patterns of the French Rhône River using Landsat ETM+ thermal infrared images. *Aquatic Sciences*, 74(3):405–414.

Webb, B. W., Hannah, D. M., Moore, R. D., Brown, L. E., and Nobilis, F. (2008). Recent advances in stream and river temperature research. *Hydrological Processes*, 22(7):902–918.

Webb, B. W. and Nobilis, F. (2007). Long-term changes in river temperature and the influence of climatic and hydrological factors. *Hydrological Sciences Journal*, 52(1):74–85.

Weng, Q. (2009). Thermal infrared remote sensing for urban climate and environmental studies: Methods, applications, and trends. *ISPRS Journal of Photogrammetry and Remote Sensing*, 64(4):335–344.

Appendix A

R Codes

A.1 Linear regression

```r
# DATA reading
pos_bouee=read.csv("GCP_ArrouxBourbince_L93.csv",sep=",",stringsAsFactors = F)
temp_bouee=read.csv("temperature_sondes.csv",sep=",",stringsAsFactors = F)


# Buffer ring created with QGIS
ring = read_sf("ring_buoy.shp")
st_crs(ring)

ring_comp = merge(ring,temp_bouee, by = "ID") # merge by ID
ring_arroux = filter(ring_comp,site=="Arroux") # filter "Arroux"


# Extract buffer ring data from raster
VARIOCAM_AR = raster("VARIOCAM_aller_retour.tif")
T_VAR  = raster::extract(VARIOCAM_AR,ring_arroux, fun = mean ,df=TRUE)
T_VAR$VARIOCAM_aller_retour[T_VAR$VARIOCAM_aller_retour %in% 1.00000] <- NA

df0 = data.frame(ID = T_VAR[,1], T_buoy = ring_arroux[,7], T_TIR = T_VAR[,2] )
df = data.frame(ID = df0[,1], T_buoy = df0[,2], T_TIR = df0[,4] )


# model VAriocam


modele_V = lm( T_TIR ~ T_buoy , df)
summary(modele_V)


equation = function(x) {
  lm_coef <- list(a = round(coef(x)[[1]], digits = 2),
                  b = round(coef(x)[[2]], digits = 2),
                  r2 = round(summary(x)$r.squared, digits = 2));
  lm_eq <- substitute(italic(y) ==  a + (b) %.% italic(x)*","~~italic(R)^2~"="~r2,lm_coef)
  as.character(as.expression(lm_eq));
}


p10 <- ggplot(df, aes(x=T_buoy, y=T_TIR)) +
  geom_point(shape=19,size=2) +
  geom_smooth(method=lm, se=TRUE) +
  theme_bw(base_size = 16)+
  scale_x_continuous(name = "Real temperature [C?]",limits = c(28.5,31)) +
  scale_y_continuous(name = "TIR temperature [C?]",limits = c(30,40)) +
  annotate("text", x = 30, y = 36, label = equation(modele_V),size=5, parse = TRUE)
```

A.2 Bland-Altman

```r
# DATA reading
pos_bouee=read.csv("GCP_ArrouxBourbince_L93.csv",sep=",",stringsAsFactors = F)
temp_bouee=read.csv("temperature_sondes.csv",sep=",",stringsAsFactors = F)

ring = read_sf("ring_buoy.shp")
st_crs(ring) # ok L93

ring_comp = merge(ring,temp_bouee, by = "ID")
ring_arroux = filter(ring_comp,site=="Arroux")


# Extract buffer ring data from raster
VARIOCAM_AR = raster("VARIOCAM_aller_retour.tif")
FLIR_AR = raster("FLIR_aller_retour.tif")

T_VAR  = raster::extract(VARIOCAM_AR,ring_arroux,fun = mean,df=TRUE)
T_FAR  = raster::extract(FLIR_AR,ring_arroux,fun = mean,df=TRUE)

T_FAR$FLIR_aller_retour[T_FAR$FLIR_aller_retour %in% 1.00000] <- NA

DF = data_frame(T_VAR$VARIOCAM_aller_retour,
                ring_arroux$meanT,
                MEAN = (T_VAR$VARIOCAM_aller_retour+ring_arroux$meanT)/2,
                DIFF = ring_arroux$meanT- T_VAR$VARIOCAM_aller_retour)

DF1 = data_frame (T_FAR$FLIR_aller_retour,
                  ring_arroux$meanT,
                  MEAN = (T_FAR$FLIR_aller_retour+ring_arroux$meanT)/2,
                  DIFF = ring_arroux$meanT- T_FAR$FLIR_aller_retour)


################################### VARIOCAM ##############################################

x = DF$MEAN
y = DF$DIFF


#regression
lm1<-lm(y~x)
lm1
summary(lm1)


#Bland Altman diagram
E = bland.altman.plot(DF$`ring_arroux$meanT`,
                      DF$`T_VAR$VARIOCAM_aller_retour`,
                      xlab="Means", ylab="Differences",silent=FALSE)
E+ abline(lm1)


################################### FLIR ##############################################

x1 = DF1$MEAN
```

```r
y1 = DF1$DIFF


#regression
lm2<-lm(y1~x1)
lm2
summary(lm2)


#Bland Altman diagram
G = bland.altman.plot(DF1$`ring_arroux$meanT`,
                      DF1$`T_FAR$FLIR_aller_retour`,
                      xlab="Means", ylab="Differences",silent=FALSE)
G + abline(lm2)
```

A.3 Longitudinal temperature profile

```r
#----- data reading ------------------#
center_point = st_read("CP_VARIOCAM_AR.shp",stringsAsFactors = F )

VARIOCAM_AR = raster("VARIOCAM_aller_retour.tif")

T_profil_VAR  = raster::extract(VARIOCAM_AR,
                                center_point,
                                buffer = 1,
                                fun = mean,
                                df = TRUE)

save(T_profil_VAR,file = "extract_VAR.RData")

T_profil_VAR$VARIOCAM_aller_retour[T_profil_VAR$VARIOCAM_aller_retour %in% 1.00000] <- NA


#----- Linear model correction -------#
p = 10.3449
m = 0.7284

T_profil_VAR$VARIOCAM_aller_retour = ((T_profil_VAR$VARIOCAM_aller_retour) - p ) / m

T_profil_VAR1 = cbind.data.frame(classe = center_point$id ,
                                 distance = center_point$distance/1000,
                                 T_TIR = T_profil_VAR$VARIOCAM_aller_retour)

T_VAR_Filter = filter(T_profil_VAR1, classe == 1)
T_VAR_Filter = filter(T_VAR_Filter, T_TIR > 27)


#--------- ad Buoys --------------------#
pos_bouee=read.csv("GCP_ArrouxBourbince_L93.csv",sep=",",stringsAsFactors = F)

temp_bouee=read.csv("temperature_sondes.csv",sep=",",stringsAsFactors = F)

dist_bouee=read.csv("distance_sondes.csv",sep=";",stringsAsFactors = F)
colnames(dist_bouee)=c("ID","distance")

Therm_complet = merge(pos_bouee,temp_bouee, by = "ID")

Therm_bouee_Arroux = filter(Therm_complet,site=="Arroux")

PDT = merge(Therm_bouee_Arroux ,dist_bouee, by = "ID")

PDT[,9] = PDT[,9]/1000


# -------- graph ------------------------#
C = ggplot(PDT,aes(x=distance,y=meanT))+
  geom_point(shape = 24,fill="blue",size=4)+
  ggtitle("Longitudinal temperature profile") +
  scale_x_continuous(breaks = seq(0,35,5), limits = c(0,36))+
  geom_line(T_VAR_Filter,mapping = aes(x=distance,y=T_TIR))
```

```
C = C + labs(x = "Distance (km)",y = "Water temperature (C?)")


# ------- moving mmean --------------------
mean_VAR = runmean(T_VAR_Filter$T_TIR,alg ="C",20)
Profil_VAR_mean = data.frame(mean_VAR,T_VAR_Filter$distance)


# Graph
D = ggplot(PDT,aes(x=distance,y=meanT))+
  geom_point(shape = 24,fill="blue",size=4)+
  ggtitle("Longitudinal temperature profile") +
  scale_x_continuous(breaks = seq(0,35,5), limits = c(0,36))+
  geom_line(Profil_VAR_mean,mapping = aes(x=T_VAR_Filter.distance,y=mean_VAR))
D = D + labs(x = "Distance upstream (km)",y = "Water Temperature (C?)")


#--------- moving median ------------------#
med_VAR = runmed(T_VAR_Filter$T_TIR,
                 51,
                 endrule = c("median"),
                 algorithm = NULL,
                 na.action = c("+Big_alternate"))

Profil_VAR_med = data.frame(med_VAR,T_VAR_Filter$distance)


# Graph
D = ggplot(PDT,aes(x=distance,y=meanT))+
  geom_point(shape = 24,fill="blue",size=4)+
  ggtitle("Longitudinal temperature profile") +
  scale_x_continuous(breaks = seq(0,35,5), limits = c(0,36))+
  geom_line(Profil_VAR_med,mapping = aes(x=T_VAR_Filter.distance,y=med_VAR))
D = D + labs(x = "Distance upstream (km)",y = "Water Temperature (C?)")
```

A.4 Rasters comparison

```r
#------buyos data-----#

F13 <- data.frame(N= 6600768.743, E = 776690.361)
F15 <- data.frame(N= 6602798.333, E = 779528.501)


#------linear regression data-----#
p=10.3449
m=0.7284


#-------------------------------------------------------------------------------------------#
#--------RGB Bourbince tributary----------#
RGB_F13 <- stack("Raster/RGB_F13.tif")
p1 <- ggRGB(RGB_F13, r=1, g=2,b=3)+
  theme_void()+
  geom_point(data = F13, aes(x = E, y = N), size = 3, color = "red")+
  geom_text_repel(aes(x= F13$E, y= F13$N, label="F13\n 29.70°C"),
                  fontface = 'bold',
                  point.padding = unit(0.25, "lines"),
                  box.padding = unit(0.25, "lines"),
                  nudge_y = 0.1,
                  size=7)


#------raster VAR Bourbince tributary-----#
VAR_F13 <- stack("Raster/VAR_F13.tif")
VAR_F13= (VAR_F13-p)/m
VAR_F13_treat <- clamp(VAR_F13, upper=35.647, lower=27.25, useValues=FALSE)
br <- seq(27,  36, 1)
cols <- viridis(n=9,option="C")
p2 <-ggRGB(RGB_F13, r=1, g=2, b=3)+ggR(VAR_F13_treat,ggLayer=T,geom_raster=T)+
  scale_fill_gradientn(colours=cols,
                       breaks=br,  limits=c(27, 36), na.value = NA,
                       guide=guide_colorbar(nbin=100, barheight=unit(0.60, "npc"),
                                            barwidth = unit(0.05, "npc"),
                                            label.hjust=1))+
  theme_void()+
  labs(fill = "T(°C)")+
  theme(legend.title = element_text(size = 16),
    legend.text=  element_text( size = 15))


#-----raster FAR Bourbince tributary-----#
FAR_F13 <- stack("Raster/FAR_F13.tif")
FAR_F13= (FAR_F13-p)/m
FAR_F13_treat <- clamp(FAR_F13, upper=39.63, lower=27.01, useValues=FALSE)
br <- seq(31,  40, 1)
cols <- viridis(n=9,option="C")
p3 <-ggRGB(RGB_F13, r=1, g=2, b=3)+ggR(FAR_F13_treat,ggLayer=T,geom_raster=T)+
  scale_fill_gradientn(colours=cols,
                       breaks=br,  limits=c(31, 40), na.value = NA,
                       guide=guide_colorbar(nbin=100, barheight=unit(0.60, "npc"),
```

```
                                          barwidth = unit(0.05, "npc"),
                                          label.hjust=1, raster = T))+
  theme_void()+
  labs(fill = "T(°C)")+
  theme(legend.title = element_text(size = 16),
        legend.text=  element_text( size = 15))


#-----difference Bourbince tributary----#
library(dichromat)
FAR_F13_adapted <- projectRaster(FAR_F13_treat, VAR_F13_treat)
diff_F13 <- VAR_F13-FAR_F13_adapted
diff_F13 <- clamp(diff_F13, lower=-30, useValues=FALSE)
br <- seq(-13,  3, 2)
cols <- c("#08306B", "#08306B","#2171B5" , "#4292C6",
          "#6BAED6", "#9ECAE1", "#D9D95F", "#F6F630")
p4 <-ggRGB(RGB_F13, r=1, g=2, b=3)+ggR(diff_F13,ggLayer=T,geom_raster=T)+
  scale_fill_gradientn(colours=cols,
                       breaks=br,  limits=c(-13, 3), na.value = NA,
                       guide=guide_colorbar(nbin=100, barheight=unit(0.60, "npc"),
                                            barwidth = unit(0.05, "npc"),
                                            label.hjust=1))+
  theme_void()+
  labs(fill = "T(°C)")+
  theme(legend.title = element_text(size = 16),
        legend.text=  element_text( size = 15))

#----histograms Bourbince tributary-----#
range=c(32,"",33,"",34,"",35,"",36,"",37,"",38,"",39,"",40)
a<- hist(VAR_F13_treat, ylim=c(0,40000), xlim=c(27,36),
         ylab= "Frequency of pixels", xlab= "Temperature (°C)",
         main="", breaks=18, col= "darkslategray", xaxt="n", cex.lab=1.3, cex.axis=1.5)
axis(side=1, at=seq(27,36, 0.5), labels=seq(27,36,0.5), cex.axis=1.5)
b <- hist(FAR_F13_treat, ylim=c(0,40000), xlim=c(32,40),
          ylab= "Frequency of pixels", xlab= "Temperature (°C)",
          main="", breaks=16, col= "darkslategray", xaxt="n", cex.lab=1.3, cex.axis=1.5)
axis(side=1, at=seq(32,40, 0.5), labels=range, cex.axis=1.5)


#-------------------------------------------------------------------------------------------#
#--------RGB Gueugnon bridge----------#
RGB_pont <- stack("Raster/RGB_zone_chaude_pont.tif")
p1 <- ggRGB(RGB_pont, r=1, g=2,b=3)+
  theme_void()


#--------raster Gueugnon bridge-------#
VAR_pont <- stack("Raster/VAR_zone_chaude_pont.tif")
VAR_pont= (VAR_pont-p)/m
VAR_pont_treat <- clamp(VAR_pont, upper=35.647, lower=27.25, useValues=FALSE)
br <- seq(27,  36, 1)
cols <- viridis(n=9,option="C")
p2 <-ggRGB(RGB_pont, r=1, g=2, b=3)+ggR(VAR_pont_treat,ggLayer=T,geom_raster=T)+
```

```
  scale_fill_gradientn(colours=cols,
                       breaks=br,  limits=c(27, 36), na.value = NA,
                       guide=guide_colorbar(nbin=100, barheight=unit(0.60, "npc"),
                                            barwidth = unit(0.05, "npc"),
                                            label.hjust=1, raster = T))+
  theme_void()+
  labs(fill = "T(°C)")+
  theme(legend.title = element_text(size = 16),
        legend.text=  element_text( size = 15))


#--------raster Gueugnon bridge-------#
FAR_pont<- stack("Raster/FLIR_zone_chaude_pont.tif")
FAR_pont= (FAR_pont-p)/m
FAR_pont_treat <- clamp(FAR_pont, upper=39.63, lower=27.01, useValues=FALSE)
br <- seq(32,  40, 1)
cols <- viridis(n=8,option="C")
p3 <-ggRGB(RGB_pont, r=1, g=2, b=3)+ggR(FAR_pont_treat,ggLayer=T,geom_raster=T)+
  scale_fill_gradientn(colours=cols,
                       breaks=br,  limits=c(32, 40), na.value = NA,
                       guide=guide_colorbar(nbin=100, barheight=unit(0.60, "npc"),
                                            barwidth = unit(0.05, "npc"),
                                            label.hjust=1, raster = T))+
  theme_void()+
  labs(fill = "T(°C)")+
  theme(legend.title = element_text(size = 16),
        legend.text=  element_text( size = 15))


#-------difference Gueugnon bridge-----#
FAR_pont_adapted <- projectRaster(FAR_pont_treat, VAR_pont_treat)
diff_pont <- VAR_pont_treat - FAR_pont_adapted
br <- seq(-13,  0, 2)
cols <- c("#08306B", "#08306B","#2171B5" , "#4292C6", "#6BAED6", "#9ECAE1")
p4 <-ggRGB(RGB_pont, r=1, g=2, b=3)+ggR(diff_pont,ggLayer=T,geom_raster=T)+
  scale_fill_gradientn(colours=cols,
                       breaks=br,  limits=c(-11, -1), na.value = NA,
                       guide=guide_colorbar(nbin=100, barheight=unit(0.60, "npc"),
                                            barwidth = unit(0.05, "npc"),
                                            label.hjust=1, raster = T))+
  theme_void()+
  labs(fill = "T(°C)")+
  theme(legend.title = element_text(size = 16),
        legend.text=  element_text( size = 15))


#----histograms Gueugnon bridge-----#
range=c(32,"",33,"",34,"",35,"",36,"",37,"",38,"",39,"",40)
a<- hist(VAR_pont_treat, ylim=c(0,20000), xlim=c(27,36),
         ylab= "Frequency of pixels", xlab= "Temperature (°C)",
         main="", breaks=18, col= "darkslategray", xaxt="n", cex.lab=1.3, cex.axis=1.5)
axis(side=1, at=seq(27,36, 0.5), labels=seq(27,36,0.5), cex.axis=1.5)
b <- hist(FAR_pont_treat, ylim=c(0,20000), xlim=c(32,40),
```

```
          ylab= "Frequency of pixels", xlab= "Temperature (°C)",
          main="", breaks=16, col= "darkslategray", xaxt="n", cex.lab=1.3, cex.axis=1.5)
axis(side=1, at=seq(32,40, 0.5), labels=range, cex.axis=1.5)


#-------------------------------------------------------------------------------------------#
#--------RGB F15----------#
RGB_F15 <- stack("Raster/RGB_F15.tif")
p1 <- ggRGB(RGB_F15, r=1, g=2,b=3)+
  theme_void()+
  geom_point(data = F15, aes(x = E, y = N), size = 3, color = "red")+
  geom_text_repel(aes(x= F15$E, y= F15$N, label="F15\n 30.12°C"),
                  fontface = 'bold',
                  point.padding = unit(0.25, "lines"),
                  box.padding = unit(0.25, "lines"),
                  nudge_y = 0.1,
                  size=7)


#--------raster VAR F15-------#
VAR_F15 <- stack("Raster/VAR_F15.tif")
VAR_F15= (VAR_F15-p)/m
VAR_F15_treat <- clamp(VAR_F15, upper=35.647, lower=27.25, useValues=FALSE)
br <- seq(27,  36, 1)
cols <- viridis(n=9,option="C")
p2 <-ggRGB(RGB_F15, r=1, g=2, b=3)+ggR(VAR_F15_treat,ggLayer=T,geom_raster=T)+
  scale_fill_gradientn(colours=cols,
                       breaks=br,  limits=c(27, 36), na.value = NA,
                       guide=guide_colorbar(nbin=100, barheight=unit(0.60, "npc"),
                                            barwidth = unit(0.05, "npc"), label.hjust=1))+
  theme_void()+
  labs(fill = "T(°C)")+
  theme(legend.title = element_text(size = 16),
        legend.text=  element_text( size = 15))


#--------raster FAR F15-------#
FAR_F15 <- stack("Raster/FAR_F15.tif")
FAR_F15= (FAR_F15-p)/m
FAR_F15_treat <- clamp(FAR_F15, upper=39.63, lower=27.01, useValues=FALSE)
br <- seq(28,  40, 1)
cols <- viridis(n=12,option="C")
p3 <-ggRGB(RGB_F15, r=1, g=2, b=3)+ggR(FAR_F15_treat,ggLayer=T,geom_raster=T)+
  scale_fill_gradientn(colours=cols,
                       breaks=br,  limits=c(28, 40), na.value = NA,
                       guide=guide_colorbar(nbin=100, barheight=unit(0.60, "npc"),
                                            barwidth = unit(0.05, "npc"),
                                            label.hjust=1, raster = T))+
  theme_void()+
  labs(fill = "T(°C)")+theme(legend.title = element_text(size = 16),
                             legend.text=  element_text( size = 15))
```

```
#---------difference F15----------#
FAR_F15_adapted <- projectRaster(FAR_F15_treat, VAR_F15_treat)
diff_F15 <- VAR_F15_treat-FAR_F15_adapted
br <- seq(-12,  3, 2)
cols <- c("#08306B", "#08306B","#2171B5" , "#4292C6",
          "#6BAED6", "#9ECAE1", "#D9D95F", "#F6F630")
p4 <-ggRGB(RGB_F15, r=1, g=2, b=3)+ggR(diff_F15,ggLayer=T,geom_raster=T)+
  scale_fill_gradientn(colours=cols,
                       breaks=br,  limits=c(-12, 3), na.value = NA,
                       guide=guide_colorbar(nbin=100, barheight=unit(0.60, "npc"),
                                            barwidth = unit(0.05, "npc"),
                                            label.hjust=1))+
  theme_void()+
  labs(fill = "T(°C)")+
  theme(legend.title = element_text(size = 16),
                            legend.text=  element_text( size = 15))


#----------histograms F15---------#
range=c(28, "", 29, "", 30, "",31, "" ,32,"",33,"",34,"",35,"",36,"",37,"",38,"",39,"",40)
a<- hist(VAR_F15_treat, ylim=c(0,30000), xlim=c(27,36),
         ylab= "Frequency of pixels", xlab= "Temperature (°C)",
         main="", breaks=18, col= "darkslategray", xaxt="n", cex.lab=1.3, cex.axis=1.5)
axis(side=1, at=seq(27,36, 0.5), labels=seq(27,36,0.5), cex.axis= 1.5)
b <- hist(FAR_F15_treat, ylim=c(0,30000), xlim=c(28,40),
          ylab= "Frequency of pixels", xlab= "Temperature (°C)",
          main="", breaks=24, col= "darkslategray", xaxt="n", cex.lab=1.3, cex.axis=1.5)
axis(side=1, at=seq(28, 40, 0.5), labels=range, cex.axis=1.4)
```

Appendix B

Linear regression results

B.1 Correction model

(a) FLIR outward flight

```
> print(modele_V)

Call:
lm(formula = T_TIR ~ T_buoy, data = df)

Coefficients:
(Intercept)       T_buoy
    16.3047       0.6387

> summary(modele_V)

Call:
lm(formula = T_TIR ~ T_buoy, data = df)

Residuals:
      1       4       5       6       7       9      10
 1.2847  5.2188 -2.2052 -2.1519 -0.8036 -1.6688  0.3261

Coefficients:
            Estimate Std. Error t value Pr(>|t|)
(Intercept)  16.3047    40.3113   0.404    0.703
T_buoy        0.6387     1.3637   0.468    0.659

Residual standard error: 2.895 on 5 degrees of freedom
  (3 observations deleted due to missingness)
Multiple R-squared:  0.04203,   Adjusted R-squared:  -0.1496
F-statistic: 0.2194 on 1 and 5 DF,  p-value: 0.6592
```

(b) VARIOCAM outward flight

```
> print(modele_V)

Call:
lm(formula = T_TIR ~ T_buoy, data = df)

Coefficients:
(Intercept)       T_buoy
    12.0491       0.6625

> summary(modele_V)

Call:
lm(formula = T_TIR ~ T_buoy, data = df)

Residuals:
     Min       1Q   Median       3Q      Max
-0.64965 -0.03673  0.08102  0.11456  0.41025

Coefficients:
            Estimate Std. Error t value Pr(>|t|)
(Intercept)  12.0491     4.5763   2.633  0.03890 *
T_buoy        0.6625     0.1544   4.292  0.00514 **
---
Signif. codes:  0 ‘***’ 0.001 ‘**’ 0.01 ‘*’ 0.05 ‘.’ 0.1 ‘ ’ 1

Residual standard error: 0.3334 on 6 degrees of freedom
  (2 observations deleted due to missingness)
Multiple R-squared:  0.7543,    Adjusted R-squared:  0.7133
F-statistic: 18.42 on 1 and 6 DF,  p-value: 0.00514
```

(c) FLIR return flight

```
> print(modele_V)

Call:
lm(formula = T_TIR ~ T_buoy, data = df)

Coefficients:
(Intercept)       T_buoy
    -16.167        1.742

> summary(modele_V)

Call:
lm(formula = T_TIR ~ T_buoy, data = df)

Residuals:
      3       4       5       6       7       8      10
-1.9151  0.9498 -1.9644  0.6667  0.4407  0.6139  1.2085

Coefficients:
            Estimate Std. Error t value Pr(>|t|)
(Intercept) -16.1667    23.4651  -0.689   0.5215
T_buoy        1.7421     0.7981   2.183   0.0808 .
---
Signif. codes:  0 ‘***’ 0.001 ‘**’ 0.01 ‘*’ 0.05 ‘.’ 0.1 ‘ ’ 1

Residual standard error: 1.477 on 5 degrees of freedom
  (3 observations deleted due to missingness)
Multiple R-squared:  0.488,     Adjusted R-squared:  0.3856
F-statistic: 4.765 on 1 and 5 DF,  p-value: 0.08082
```

(d) VARIOCAM return flight

```
> print(modele_V)

Call:
lm(formula = T_TIR ~ T_buoy, data = df)

Coefficients:
(Intercept)       T_buoy
    10.3937       0.7302

> summary(modele_V)

Call:
lm(formula = T_TIR ~ T_buoy, data = df)

Residuals:
     Min       1Q   Median       3Q      Max
-0.2633 -0.2087 -0.1081  0.0488  0.6372

Coefficients:
            Estimate Std. Error t value Pr(>|t|)
(Intercept)  10.3937     3.7961   2.738 0.025528 *
T_buoy        0.7302     0.1279   5.710 0.000449 ***
---
Signif. codes:  0 ‘***’ 0.001 ‘**’ 0.01 ‘*’ 0.05 ‘.’ 0.1 ‘ ’ 1

Residual standard error: 0.3093 on 8 degrees of freedom
Multiple R-squared:  0.803,     Adjusted R-squared:  0.7783
F-statistic:  32.6 on 1 and 8 DF,  p-value: 0.0004493
```

(e) FLIR return flight

```
> print(modele_V)

Call:
lm(formula = T_TIR ~ T_buoy, data = df)

Coefficients:
(Intercept)       T_buoy
    16.1882       0.6393

> summary(modele_V)

Call:
lm(formula = T_TIR ~ T_buoy, data = df)

Residuals:
    Min      1Q  Median      3Q     Max
-1.6060 -1.3251  0.2181  1.2173  2.0776

Coefficients:
            Estimate Std. Error t value Pr(>|t|)
(Intercept)  16.1882    20.0297   0.808    0.446
T_buoy        0.6393     0.6771   0.944    0.377

Residual standard error: 1.506 on 7 degrees of freedom
  (1 observation deleted due to missingness)
Multiple R-squared:  0.113,     Adjusted R-squared:  -0.01374
F-statistic: 0.8915 on 1 and 7 DF,  p-value: 0.3765
```

(f) VARIOCAM return flight

```
> print(modele_V)

Call:
lm(formula = T_TIR ~ T_buoy, data = df)

Coefficients:
(Intercept)       T_buoy
    10.3449       0.7284

> summary(modele_V)

Call:
lm(formula = T_TIR ~ T_buoy, data = df)

Residuals:
     Min       1Q   Median       3Q      Max
-0.21803 -0.13674 -0.06949  0.12646  0.42395

Coefficients:
            Estimate Std. Error t value Pr(>|t|)
(Intercept) 10.34489    2.62948   3.934  0.00433 **
T_buoy       0.72836    0.08858   8.222 3.58e-05 ***
---
Signif. codes:  0 ‘***’ 0.001 ‘**’ 0.01 ‘*’ 0.05 ‘.’ 0.1 ‘ ’ 1

Residual standard error: 0.2142 on 8 degrees of freedom
Multiple R-squared:  0.8942,    Adjusted R-squared:  0.881
F-statistic: 67.61 on 1 and 8 DF,  p-value: 3.583e-05
```

Figure (B.1) Tables linear regression models

B.2 Bland-Altman

(a) FLIR outward and return flight

```
> lm2

Call:
lm(formula = y1 ~ x1)

Coefficients:
(Intercept)           x1
    23.1887      -0.8879

> summary(lm2)

Call:
lm(formula = y1 ~ x1)

Residuals:
    Min      1Q  Median      3Q     Max
-1.7037 -0.6191 -0.5019  0.5552  1.9708

Coefficients:
            Estimate Std. Error t value Pr(>|t|)
(Intercept)  23.1887    14.8576   1.561   0.1626
x1           -0.8879     0.4593  -1.933   0.0945 .
---
Signif. codes:  0 '***' 0.001 '**' 0.01 '*' 0.05 '.' 0.1 ' ' 1

Residual standard error: 1.241 on 7 degrees of freedom
  (1 observation deleted due to missingness)
Multiple R-squared:  0.348,     Adjusted R-squared:  0.2549
F-statistic: 3.737 on 1 and 7 DF,  p-value: 0.0945
```

(b) VARIOCAM outward and return flight

```
> lm1

Call:
lm(formula = y ~ x)

Coefficients:
(Intercept)            x
   -10.5029       0.2667

> summary(lm1)

Call:
lm(formula = y ~ x)

Residuals:
    Min      1Q  Median      3Q     Max
-0.5053 -0.1149  0.0543  0.1283  0.2896

Coefficients:
            Estimate Std. Error t value Pr(>|t|)
(Intercept) -10.5029     3.5809  -2.933   0.0189 *
x             0.2667     0.1162   2.296   0.0508 .
---
Signif. codes:  0 '***' 0.001 '**' 0.01 '*' 0.05 '.' 0.1 ' ' 1

Residual standard error: 0.2453 on 8 degrees of freedom
Multiple R-squared:  0.3971,    Adjusted R-squared:  0.3218
F-statistic:  5.27 on 1 and 8 DF,  p-value: 0.05081
```

(c) Corrected FLIR outward and return flight

```
> lm2

Call:
lm(formula = y1 ~ x1)

Coefficients:
(Intercept)           x1
     39.185       -1.325

> summary(lm2)

Call:
lm(formula = y1 ~ x1)

Residuals:
    Min      1Q  Median      3Q     Max
-1.7645 -0.6966 -0.5785  0.8571  2.2016

Coefficients:
            Estimate Std. Error t value Pr(>|t|)
(Intercept)  39.1848    10.5810   3.703  0.00762 **
x1           -1.3250     0.3575  -3.707  0.00759 **
---
Signif. codes:  0 '***' 0.001 '**' 0.01 '*' 0.05 '.' 0.1 ' ' 1

Residual standard error: 1.369 on 7 degrees of freedom
  (1 observation deleted due to missingness)
Multiple R-squared:  0.6625,    Adjusted R-squared:  0.6143
F-statistic: 13.74 on 1 and 7 DF,  p-value: 0.007587
```

(d) Corrected VARIOCAM outward and return flight

```
> lm1

Call:
lm(formula = y ~ x)

Coefficients:
(Intercept)            x
    1.70517     -0.05741

> summary(lm1)

Call:
lm(formula = y ~ x)

Residuals:
      Min       1Q   Median       3Q      Max
-0.60001 -0.13271  0.05852  0.14514  0.35004

Coefficients:
            Estimate Std. Error t value Pr(>|t|)
(Intercept)  1.70517    3.50636   0.486     0.64
x           -0.05741    0.11813  -0.486     0.64

Residual standard error: 0.2898 on 8 degrees of freedom
Multiple R-squared:  0.02867,   Adjusted R-squared:  -0.09274
F-statistic: 0.2362 on 1 and 8 DF,  p-value: 0.64
```

Figure (B.2) Bland-Altman linear regression models